

---

Electronic Thesis and Dissertation Repository

---

9-30-2019 10:00 AM

# Schrödinger Filtering: A Novel Technique for Removing Gradient Artifact from Electroencephalography Data Acquired during Functional Magnetic Resonance Imaging

Gabriel Bruno Benigno, *The University of Western Ontario*

Supervisor: Menon, Ravi S., *The University of Western Ontario*

A thesis submitted in partial fulfillment of the requirements for the Master of Science degree in Medical Biophysics

© Gabriel Bruno Benigno 2019

Follow this and additional works at: <https://ir.lib.uwo.ca/etd>



Part of the [Signal Processing Commons](#)

---

## Recommended Citation

Benigno, Gabriel Bruno, "Schrödinger Filtering: A Novel Technique for Removing Gradient Artifact from Electroencephalography Data Acquired during Functional Magnetic Resonance Imaging" (2019). *Electronic Thesis and Dissertation Repository*. 6606.  
<https://ir.lib.uwo.ca/etd/6606>

This Dissertation/Thesis is brought to you for free and open access by Scholarship@Western. It has been accepted for inclusion in Electronic Thesis and Dissertation Repository by an authorized administrator of Scholarship@Western. For more information, please contact [wlsadmin@uwo.ca](mailto:wlsadmin@uwo.ca).

# Abstract

Electroencephalography (EEG) and functional magnetic resonance imaging (fMRI) are complementary modalities commonly acquired simultaneously to study brain function with high spatial and temporal resolution. The time-varying gradient fields from fMRI induce large-amplitude gradient artifacts (GRAs) that overlap in time and frequency with EEG, making GRA removal a challenge for which no satisfactory solution yet exists. We present a new GRA removal method termed Schrödinger filtering (SF). SF is based on semi-classical signal analysis in which a signal is decomposed into a series of energy-based components using the discrete spectrum of the Schrödinger operator. Using a publicly available dataset, we compared our pipeline, which features only the popular average artifact subtraction (AAS) technique and SF, to two popular pipelines. The SF pipeline outperformed across all frequency bands based on metrics of signal preservation and GRA removal. SF, when combined with AAS, is therefore effective in removing GRA from EEG data.

Keywords: Electroencephalography (EEG), functional magnetic resonance imaging (fMRI), gradient artifact, Schrödinger equation, semi-classical signal analysis (SCSA), filter, signal processing.

## Lay summary

Electroencephalography (EEG) directly measures brain activity with electrodes placed on the scalp. EEG records measurements quickly although it is unable to well-localize the sources of the activity. Functional magnetic resonance imaging (fMRI) forms a set of images of the brain over time. These images measure changes in blood flow and oxygenation that accompany brain activity. Therefore, fMRI indirectly measures brain activity. fMRI well-localizes brain activity but takes relatively long to acquire a single image. Both EEG and fMRI are non-invasive. The combined modality of simultaneous EEG and fMRI (EEG-fMRI) therefore offers the benefit of noninvasively recording brain activity with both high spatial and temporal resolution.

One unique challenge of EEG-fMRI is the gradient artifact: a large-amplitude set of signal disruptions in the EEG data caused by the interaction of the fMRI magnetic gradient fields with the EEG equipment. The gradient artifact has been studied for over a decade and numerous solutions have been proposed. However, no solution reduces the gradient artifact while preserving the underlying signal such that it is not a significant impediment to the analysis of the EEG data.

We present a new technique for removal of the gradient artifact called Schrödinger filtering. Schrödinger filtering is able to decompose a signal into a set of constituent signals, each possessing a different energy, where energy is proportional to signal amplitude. Schrödinger filtering is well-suited for gradient artifact removal because these constituent signals separately capture the signal and artifact based on energy differences.

On an online dataset, we applied a popular gradient artifact removal step called average artifact subtraction followed by Schrödinger filtering. We compared the performance of our processing pipeline to that of two other popular pipelines in terms of signal preservation and artifact removal. Our pipeline outperformed the other two. These results indicate that Schrödinger filtering is an excellent processing technique for gradient artifact removal that helps with the analysis of EEG data of EEG-fMRI.

## **Co-authorship statement**

Some sections of this thesis share content from a manuscript of which I am the major contributor. Said manuscript was submitted on July 22, 2019 for publication in the peer-reviewed academic journal NeuroImage. The reviewers requested revisions of the manuscript on September 17, 2019. On October 2, 2019, the revised manuscript was submitted. My responsibilities included pipeline and software development, data analysis and interpretation, and manuscript preparation and submission. I estimate that I solely conducted 95% of the work. The two co-authors, Ravi Menon—the principal investigator and thesis supervisor—and Hacene Serrai—the lab manager and research scientist—provided continued expertise and supervision of the study, as well as manuscript proofreading.

## Acknowledgments

I would like to thank my supervisor Ravi Menon for providing me the opportunity and resources for conducting high-quality research, and for the freedom to explore research questions of my interest. I would also like to acknowledge the fruitful discussions we had in shaping my research questions. You taught me the value of holding myself accountable during my journey as a researcher and that I have the greatest influence on my outcome. I have become a more independent researcher thanks to you.

I would also like to thank my advisory committee of Stefan Everling and Keith St. Lawrence. You have provided great counsel and advice during our meetings. Thanks also to Kathleen Petts and Umera Ali, who have been thorough and timely in their administrative assistance. Thanks to the department chair Aaron Ward, who has gone above and beyond in advising me. Thanks to the Department of Medical Biophysics as a whole for being well-organized and for welcoming me warmly. I have had an unforgettably positive experience as a student in this department.

Thank you to the lab manager and research scientist Hacene Serrai, who has been my mentor throughout the Schrödinger filtering study. We have had many long discussions in which we brainstormed how to best approach the study. Your expertise in signal processing was invaluable during these discussions. Thank you for always making yourself available despite your busy schedule. Thank you for also placing an emphasis on the never-ending process of learning in research. You have been very supportive during my time as your student, and your politeness and good nature have been a pleasure to work with.

Thank you to Meriem Laleg of King Abdullah University of Science and Technology, Saudi Arabia for answering my questions on semi-classical signal analysis (SCSA), for proofreading the SCSA sections of my manuscript and thesis, and for providing MATLAB scripts for SCSA.

Thank you to everyone in the Centre for Functional and Metabolic Mapping. At one time or another, you have been a great help to me. Special thanks go out to my lab-mates Olivia Stanley and Geoff Ngo for devoting their time to helping me throughout my journey and welcoming me to the lab. Thank you to the post-docs David Schaeffer and

Liya Ma and to Kyle Gilbert of the RF design suite for letting me bother you time and time again with technical questions.

Last but not least, thank you to my parents, to Anna, and to my family and friends. I have made friends in this department that will last a lifetime. To my parents, Anna, and the rest of my family, thank you for always being there. I sincerely could not have made it to this point without you and your unconditional love.

# Table of contents

Abstract.....	ii
Lay summary .....	iii
Co-authorship statement.....	iv
Acknowledgments .....	v
Table of contents .....	vii
List of figures .....	ix
List of acronyms .....	x
List of symbols .....	xi
List of equations .....	xiv
1 Introduction.....	1
1.1 Functional magnetic resonance imaging (fMRI).....	4
1.2 Electroencephalography (EEG).....	9
1.3 Simultaneous EEG and fMRI (EEG-fMRI) .....	13
1.3.1 fMRI artifacts in EEG-fMRI .....	14
1.3.2 EEG artifacts in EEG-fMRI .....	14
1.4 The gradient artifact .....	17
1.4.1 Gradient artifact structure.....	17
1.4.2 Gradient artifact removal methods .....	20
1.5 Schrödinger filtering.....	25
1.5.1 Semi-classical signal analysis (SCSA).....	26
1.5.2 Schrödinger filtering.....	30
1.6 Thesis overview.....	34
2 Methods .....	37

2.1	Dataset .....	37
2.2	Schrödinger filtering algorithm .....	38
2.2.1	Step 1: de-spiking .....	38
2.2.2	Step 2: global filtering .....	39
2.3	Processing pipelines .....	40
2.4	Evaluation of performance .....	43
2.4.1	Median residual activity (MRA) .....	43
2.4.2	Median fraction at slice frequencies (MFSF) .....	44
3	Results and Discussion .....	45
3.1	De-spiking .....	45
3.2	Global filtering .....	47
4	Conclusions.....	53
4.1	Summary.....	53
4.2	Limitations and future directions.....	54
	References .....	57
	Appendices .....	63
	Appendix A: Permission for reproduction of scientific figures.....	63
	Curriculum vitae.....	69

## List of figures

<b>Figure 1.1:</b> Precession of hydrogen atoms of water molecules. ....	5
<b>Figure 1.2:</b> RF tipping. ....	6
<b>Figure 1.3:</b> Fourier transform (FT) relationship between k-space and image space. ....	7
<b>Figure 1.4:</b> Schematic of the blood oxygenation level-dependent (BOLD) effect. ....	8
<b>Figure 1.5:</b> Dipoles formed by pyramidal neurons in generating the EEG signal. ....	10
<b>Figure 1.6:</b> Examples of scalp electrode configurations. ....	12
<b>Figure 1.7:</b> A common EEG-fMRI recording apparatus. ....	16
<b>Figure 1.8:</b> The gradient artifact. ....	18
<b>Figure 1.9:</b> Variation of the gradient artifact across channels. ....	19
<b>Figure 1.10:</b> Residual gradient artifact following AAS. ....	23
<b>Figure 1.11:</b> Illustration of SCSA. ....	29
<b>Figure 1.12:</b> The Schrödinger filtering algorithm. ....	33
<b>Figure 2.1:</b> Flowchart of the three gradient artifact removal pipelines. ....	42
<b>Figure 3.1:</b> Effect of de-spiking. ....	46
<b>Figure 3.2:</b> Positive impact of de-spiking in Schrödinger filtering. ....	47
<b>Figure 3.3:</b> Performances of the pipelines for channel with large residual artifact. ....	48
<b>Figure 3.4:</b> Performances of the pipelines for channel with small residual artifact. ....	49
<b>Figure 3.5:</b> MRA comparison of the three pipelines. ....	50
<b>Figure 3.6:</b> MFSF comparison of the three pipelines. ....	51
<b>Figure 3.7:</b> Preservation of increased alpha-band activity following eye-closing. ....	52

## List of acronyms

AAS	average artifact subtraction
ANC	adaptive noise cancelation
BOLD	blood oxygen level-dependent
ECG	electrocardiogram
EEG	electroencephalography
EEG-fMRI	simultaneous EEG and fMRI
EPSP	excitatory postsynaptic potential
FACET	Flexible Artifact Correction and Evaluation Toolbox
FASTR	fMRI Artifact Slice Template Removal
fMRI	functional magnetic resonance imaging
IAR	Image Artifact Reduction
IC	independent component
ICA	independent component analysis
IPSP	inhibitory postsynaptic potential
LORETA	low-resolution electromagnetic tomography
LPF	low-pass filtering
MAD	mean absolute deviation
MFSF	median fraction at slice frequencies
MRA	median residual activity
MRI	magnetic resonance imaging
MRS	magnetic resonance spectroscopy
NMR	nuclear magnetic resonance
OBS	optimal basis set
PCA	principal component analysis
RF	radiofrequency
SCSA	semi-classical signal analysis
SNR	signal-to-noise ratio

## List of symbols

$\frac{d^2}{dt^2}$	.....second-order differential operator
$\tilde{s}_h(t)$	.....reconstruction of $s(t)$ by SCSA
$\bar{Y}_{aas,off}^{band}$	.....magnitude spectral density of $y_{aas}$ for one EEG band during $T_{off}$
$\hat{Y}_{aas,on}^{(f)}$	..... power spectral density at slice frequency $\pm 1$ Hz of $y_{aas}$ during $T_{on}$
$\tilde{Y}_{ds,on}(f, N_h)$	..... magnitude spectrum of $\tilde{y}_{ds}(t)$ during $T_{on}$ for $N_h$
$\bar{Y}_{method,off}^{band}$	.....magnitude spectral density of $y_{method}$ for one EEG band during $T_{off}$
$\hat{Y}_{method,on}^{(f)}$	..... power spectral density at slice frequency $\pm 1$ Hz of $y_{method}$ during $T_{on}$
$\vec{A}$	.....surface vector of a closed loop
$\vec{a} \cdot \vec{b}$	.....dot product of two arbitrary vectors
$\vec{B}$	.....magnetic field vector
$\frac{d}{dt}$	..... first-order differential operator
$f(x, k)$	..... solutions of the continuous part of Equation 1.5.2
$h^*$	..... $h$ -value for optimal approximation of $s(t)$ by SCSA
$H_h(t)$	.....Schrödinger operator
$h^{sf}$	..... $h$ -value for optimal global filtering
$\min(f(x))$	..... minimum value of function $f(x)$
$N_h^*$	..... $N_h$ -value corresponding to $h = h^*$
$N_h^{sf}$	..... $N_h$ -value corresponding to $h = h^{sf}$
$N_h$	.....number of negative eigenvalues
$\hat{n}$	..... normal vector to a surface
$T_{off}$	..... non-contiguous intervals during which the gradients were off during scanning
$T_{on}$	..... non-contiguous intervals during which the gradients were on during scanning
$y_{aas}(t)$	.....post-AAS EEG timeseries
$Y_{ds,off}(f)$	.....magnitude spectrum of $y_{ds}(t)$ during $T_{off}$
$y_{ds}(t)$	..... fully de-spiked version of $y_{aas}(t)$
$y_{ds+}(t)$	..... positively de-spiked version of $y_{aas}(t)$

$y_{fastr}(t)$	EEG timeseries following FASTR variant pipeline
$y_I(t)$	primary Schrödinger component
$y_{ica}(t)$	$y_{aas}(t)$ following manual spatial ICA
$y_{II}(t)$	secondary Schrödinger component
$y_{method}$	one of $y_{fastr}$ , $y_{ica}$ , or $y_{sf}$
$y_{sf}(t)$	$y_{ds}(t)$ following global filtering
$\beta_1$	coefficient for weighted subtraction of $y_I(t)$ from $y_{aas}(t)$
$\beta_2$	coefficient for weighted subtraction of $y_{II}(t)$ from $y_{aas}(t)$
$\kappa_{h,n}$	modulus of the negative eigenvalues $\lambda$
$\in$	element of
$dx$	differential of $x$
$e$	Euler's number (2.71828...)
$\mathcal{E}$	induced voltage
$f$	frequency
$F$	spectral bandwidth of a sub-timeseries during global filtering
$h$	semi-classical parameter
$J(h)$	mean squared error between $s(t)$ and $\tilde{s}_h(t)$
$k$	spatial frequency (Section 1.1) or wavenumber (Section 1.5.1)
$\text{median}(f(x))$	median value of function $f(x)$
$MFSF_{method}^{(f)}$	MFSF for one slice frequency for one of the three pipelines
$MRA_{band}^{method}$	MRA for one EEG frequency band for one of the three pipelines
$n$	index of eigenvalues
$\mathbb{R}$	the set of real numbers
$R(k)$	reflection coefficient
$s(t)$	one-dimensional input signal
$t$	time
$x$	one-dimensional position
$\Delta(N_h)$	mean squared error between $\tilde{Y}_{ds,on}(f, N_h)$ and $Y_{ds,off}(f)$
$\theta$	angle between $\vec{B}$ and $\hat{n}$
$\lambda$	eigenvalue from Schrödinger equation

$\Phi$  .....magnetic flux  
 $\psi(t)$  ..... eigenfunction on which  $H_n(t)$  operates

## List of equations

$$\mathcal{E} = -\frac{d\Phi}{dt} = -\frac{d}{dt}(\vec{B} \cdot \vec{A}) = -\frac{d}{dt}(BA \cos \theta) \dots(1.3.1) \dots \text{induced voltage from EEG-fMRI}$$

$$H_h(t)\psi(t) = \lambda\psi(t) \dots(1.5.1) \dots \text{Schrödinger equation}$$

$$H_h(t) = -h^2 \frac{d^2}{dt^2} - s(t) \dots(1.5.2) \dots \text{Schrödinger operator}$$

$$s(t) = \frac{2i}{\pi} \int_{-\infty}^{+\infty} kR(k)f^2(t,k)dk + 4 \sum_{n=1}^N \kappa_{h,n} \psi_{h,n}^2 \dots(1.5.3) \dots \text{Deift-Trubowitz formula}$$

$$s(t) = 4 \sum_{n=1}^{N_h} \kappa_{h,n} \psi_{h,n}^2 \dots(1.5.4) \dots \text{Deift-Trubowitz formula for reflectionless potential}$$

$$\tilde{s}_h(t) = 4h \sum_{n=1}^{N_h} \kappa_{h,n} \psi_{h,n}^2(t) \dots(1.5.5) \dots \text{Schrödinger series}$$

$$J(h) = \frac{1}{M} \sum_{m=1}^M (s(t) - \tilde{s}_h(t))^2 \dots(1.5.6a) \dots \text{mean square error between } s(t) \text{ and } \tilde{s}_h(t)$$

$$J(h^*) = \min(J(h)) \dots(1.5.6b) \dots \text{minimum of } J(h)$$

$$y_{ds+}(t) = y_{aas}(t) - \beta_1 y_I(t) - \beta_2 y_{II}(t) \dots(1.5.7) \dots \text{positive de-spiking}$$

$$\Delta(N_h) = \frac{1}{F} \sum_f \left( \tilde{Y}_{ds,on}(f, N_h) - Y_{ds,off}(f) \right)^2 \dots(1.5.8a) \dots \text{mean square error for } N_h^{sf} \text{ determination}$$

$$\Delta(N_h^{sf}) = \min(\Delta(N_h)) \dots(1.5.8b) \dots \text{minimum of } \Delta(N_h)$$

$$MRA_{method}^{band} = \text{median} \left( \frac{\bar{y}_{method,off}^{band} - \bar{y}_{aas,off}^{band}}{\bar{y}_{aas,off}^{band}} \right) \dots(2.1) \dots \text{MRA for one EEG frequency band for one of the three pipelines}$$

$$MFSF_{method}^{(f)} = \text{median} \left( \frac{\hat{Y}_{method,on}^{(f)}}{\hat{Y}_{aas,on}^{(f)}} \right) \dots(2.2) \dots \text{MFSF for one slice frequency } \pm 1 \text{ Hz for one of the three pipelines}$$

# 1 Introduction

The human brain is one of the most complex and mysterious systems known. An information storage and transmission apparatus, it sends signals mainly using constituent cells called neurons. The human brain has an estimated one-hundred billion neurons<sup>1</sup> and one-hundred trillion neural connections<sup>2</sup>. Most important about the brain is its central agency in one's quality of life—a malfunctioning brain is costly to both the individual and the economy. With such complexity, brain disorder and disease are unfortunately inevitable. Perhaps more unfortunate is that the delicacy of the brain makes it so difficult to study effectively and noninvasively. The two most valued tools we have for such are electroencephalography (EEG) and functional MRI (fMRI). Their combined simultaneous acquisition (EEG-fMRI) is especially valuable although it comes with unique drawbacks that require solutions.

Ion fluxes in and out of neurons produce extracellular electric potentials that are noninvasively measured using the modality of EEG, in which an array of recording electrodes is placed on the scalp<sup>3</sup>. EEG has proven useful for all forms of brain study,

including those of sleep disorders<sup>4-6</sup> and epilepsy<sup>7-9</sup>. A strength of EEG is that it is able to record at a very high temporal resolution<sup>10</sup> while major weaknesses are its low spatial resolution<sup>11</sup> and low signal-to-noise ratio (SNR)<sup>12</sup>.

The fuel sources of the brain are glucose and oxygen, which are delivered via the blood. Oxygen is delivered by hemoglobin, a protein in red blood cells. Hemoglobin has magnetic properties that depend on whether oxygen is bound and to what extent<sup>13</sup>. Areas in the brain with elevated neural activity exhibit a blood supply with a greater concentration of oxygenated hemoglobin. Nuclear magnetic resonance (NMR) can differentiate hemoglobin based on its oxygenation state. Magnetic resonance imaging (MRI), which uses NMR, is thus able to indirectly map changes in neural activity over the whole brain via fMRI<sup>14-16</sup>. fMRI is the most popular modality for studying the brain, especially in cognitive neuroscience<sup>17</sup> and with some use in medicine<sup>18</sup>. Despite its fine spatial resolution, the process by which oxygen supply is increased is sluggish, limiting the temporal resolution of fMRI<sup>19</sup>.

EEG and fMRI are complementary in their strengths and weaknesses. While both modalities are non-invasive, EEG directly measures neural activity with high temporal resolution but poor spatial resolution. Conversely, fMRI indirectly does so with poor temporal resolution but high spatial resolution. Moreover, these two modalities are gold standards with respect to their strengths. Therefore, EEG-fMRI is preferred as a theoretical ultimate modality. EEG-fMRI is desirable for simply studying the brain with high spatial and temporal resolution. It is also useful for studies of neurovascular coupling, in which EEG measures neurons' electrical activity while fMRI measures their accompanying metabolics and hemodynamics<sup>20</sup>. However, combining acquisition of

these two modalities has unique weaknesses in which each modality imparts artifact on the other. The most detrimental artifact of EEG-fMRI is the gradient artifact, in which the interaction of the EEG equipment with the time-varying gradient fields of the MRI scanner induces large-amplitude distortions in the EEG signal<sup>21-24</sup>.

Several approaches for reducing the gradient artifact while preserving EEG signal have been conceived<sup>21-40</sup>, yet the gradient artifact remains an impediment to analysis of the EEG signal from EEG-fMRI<sup>41</sup>. The existing processing methods for gradient artifact removal apply linearly in either the time or frequency domains. In both these domains, the EEG signal and gradient artifact overlap, limiting these methods' effectiveness. The technique of average artifact subtraction (AAS)<sup>22</sup>—in which a local average of the artifact-contaminated signal forms an approximate template of the artifact that is subtracted from the signal—is simple and effective, although significant residual artifact remains following AAS<sup>41</sup>.

This thesis introduces a new gradient artifact removal technique called Schrödinger filtering. Schrödinger filtering is based on the new signal processing technique of semi-classical signal analysis (SCSA)<sup>42</sup>. In SCSA, an input signal is used as an attractive potential in the semi-classical Schrödinger operator, and the discrete spectrum of this operator is used to decompose the input signal into a series of energy-based components. SCSA is therefore analogous to the discrete Fourier transform, which represents an input signal as a series of sinusoids of different frequencies. SCSA is particularly suited for gradient artifact removal because it generates components that separately capture signal and artifact based on energy differences.

Schrödinger filtering adapts SCSA for gradient artifact removal in two steps.

Firstly, following AAS, the EEG signal is rid of gradient-related spikes by selectively removing so-called Schrödinger components—in particular, the high-energy components that depict the spikes. Secondly, the de-spiked signal is globally filtered by removing Schrödinger components corresponding to residual artifact. De-spiking facilitates a finer separation between components representing artifact and those representing signal. Schrödinger filtering also has the inherent benefit of denoising the signal.

To fully appreciate the multi-modal method of EEG-fMRI, each modality is introduced separately. Thus, the remainder of this introduction begins with background on the principles of fMRI and EEG and is followed with a description of EEG-fMRI. The gradient artifact is explained, and existing gradient artifact removal methods are given. Finally, Schrödinger filtering is described, beginning with a presentation of SCSA.

## **1.1 Functional magnetic resonance imaging (fMRI)**

fMRI is a type of MRI used to probe brain activity. The most common type of fMRI—*i.e.*, blood oxygenation level-dependent (BOLD) fMRI—is sensitive to changes in deoxyhemoglobin, which commonly occur with neural activity<sup>16</sup>. As such, BOLD fMRI is an indirect measure of brain activity. MRI is a family of imaging modalities used in biology and medicine. MRI has high spatial resolution and a versatile set of contrasts and applications; uses non-ionizing radiation; and is non-invasive. MRI is based on the phenomenon of NMR.

In NMR, the hydrogen atoms of water molecules can be thought of as precessing vectors—called spins—about an external and uniform magnetic field. The spins precess at the characteristic Larmor frequency. The macroscopic average of the spins—called the

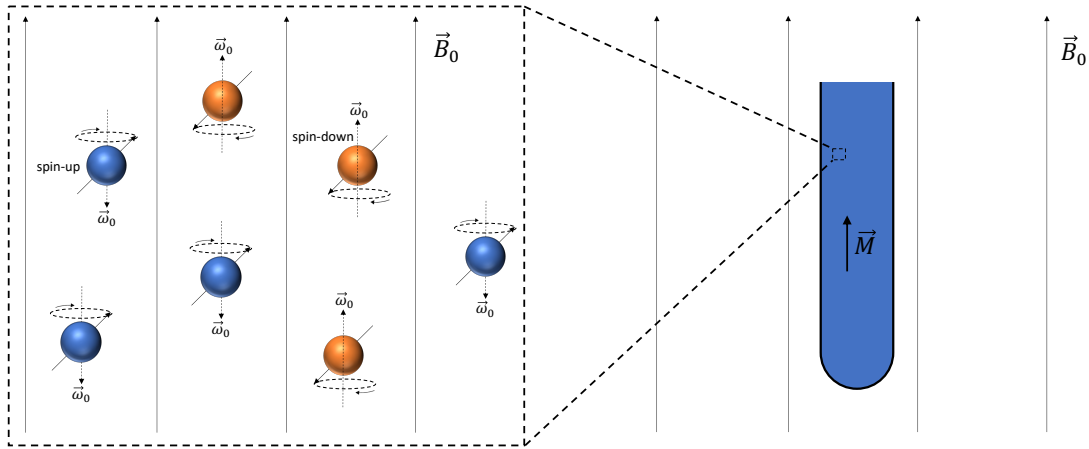


**Figure 1.1:** Precession of hydrogen atoms of water molecules.

The magnetic spins of the water hydrogen atoms precess about the external uniform magnetic field  $\vec{B}_0$  with frequency  $\vec{\omega}_0$ . In the presence of  $\vec{B}_0$ , the spins exist in either the spin-up (parallel to  $\vec{B}_0$ ) or spin-down (anti-parallel to  $\vec{B}_0$ ) state. The spin-up state is slightly lower-energy and therefore slightly more probable at room temperature, which is illustrated with four spin-up (blue spheres) and three spin-down states (orange spheres). The vector average of all the magnetic dipole moments associated with each spin surmount to a magnetization vector  $\vec{M}$  that points along  $\vec{B}_0$ .

magnetization—points along the direction of the external field (**Figure 1.1**). Application of a radiofrequency (RF) pulse, which oscillates at the Larmor frequency, tips the magnetization from equilibrium (**Figure 1.2**). The rate at which the magnetization recovers back to equilibrium is material-specific, which facilitates good tissue contrast in MRI. In the process of this recovery, the magnetization precesses and acts as a transmission antenna, giving off the NMR signal<sup>43</sup>.

The signal recorded in MRI is the NMR signal. MRI uses gradient fields to distort the field experienced by a sample in a controlled manner over so-called image space. Image space is related to spatial frequency ( $k$ ) space, called  $k$ -space, by a Fourier transform (**Figure 1.3**). This Fourier relationship allows for efficient spatial localization and discretization of the NMR signal in the sample into a grid of voxels<sup>44</sup>.

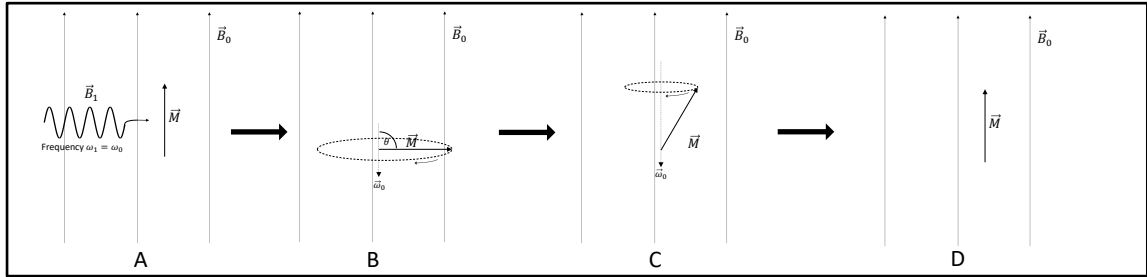


**Figure 1.2:** RF tipping.

For biologically relevant nuclei such as water protons, the Larmor precession frequency  $\omega_0$  is in the radiofrequency (RF) range. When a transiently applied electromagnetic field  $\vec{B}_1$  (A), commonly referred to as an RF pulse, has a frequency at or near  $\omega_0$ , it imparts a maximal amount of energy to the spins. This is called resonance and macroscopically corresponds to  $\vec{M}$  tipping away from the longitudinal axis of  $\vec{B}_0$  (B). The duration and amplitude of  $\vec{B}_1$  determine the tip angle  $\theta$ . While tipped,  $\vec{M}$  precesses the longitudinal axis with frequency  $\omega_0$ . Over time, the additional energy from the RF excitation is slowly lost and  $\vec{M}$  points closer toward the longitudinal axis while still precessing at  $\omega_0$  (C). After a long time,  $\vec{M}$  returns to point entirely along the longitudinal axis (D).

BOLD-contrast fMRI is the most popular type of fMRI since it has higher SNR and finer temporal resolution than its counterparts—*e.g.*, arterial spin labeling<sup>45</sup> and vascular space occupancy fMRI<sup>46</sup>. BOLD fMRI is sensitive to the regional amount of deoxyhemoglobin, which is used as an indirect measure of neural activity<sup>47</sup>. BOLD fMRI measures brain function in the form of a voxel-wise timeseries of images. From here on, fMRI will refer exclusively to BOLD fMRI.

Hemoglobin is a protein in red blood cells that stores and delivers oxygen to cells throughout the body. Hemoglobin has deoxygenated and oxygenated forms. Deoxyhemoglobin is strongly paramagnetic, giving it positive magnetic susceptibility. Oxyhemoglobin, on the other hand, is weakly diamagnetic, giving it negative susceptibility<sup>13</sup>. Tissue is also weakly diamagnetic<sup>48</sup>. Due to a susceptibility mismatch, deoxyhemoglobin weakens the magnetic field in nearby tissue, including vessels and brain tissue. The result is a greater spread of spins precessing at different frequencies in a

voxel—*i.e.*, dephasing. Dephasing shortens transverse relaxation, leading to a lower signal. In response to neural activity, there is an increased supply of oxyhemoglobin that decreases the concentration of deoxyhemoglobin in the activated brain regions, leading to a higher signal relative to the rest of the brain. This is known as BOLD contrast<sup>49</sup>.

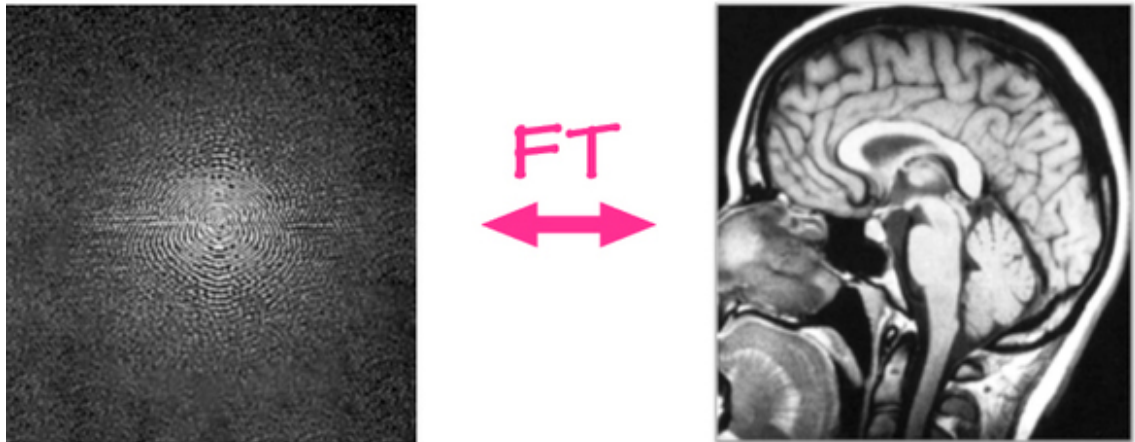


**Figure 1.3:** Fourier transform (FT) relationship between k-space and image space. Different points along k-space are sampled by applying gradient fields, which alter the sample's spins' precession frequencies and therefore their phases. The Fourier transform of the k-space spectrum is the image. (Courtesy of Allen D. Elster, MRIquestions.com. Proof of permission provided in Appendix A.)

Image acquisition in fMRI commonly uses a time-efficient technique called gradient-echo echo-planar imaging. One single image volume acquired with gradient-echo echo-planar imaging is composed of a set of stacked slices. Per slice, there is one RF pulse and numerous gradient pulses. A single run of fMRI is typically hundreds of volumes long. The result is many RF and gradient pulses applied<sup>50</sup>.

Spatial resolution in fMRI is very good, as the entire brain may be imaged at hundreds of microns to millimeters per voxel. Spatial resolution comes with trade-offs in SNR and temporal resolution, however. The lower limit of effective spatial resolution in

fMRI is in fact a few hundred microns due to the spacing of the microvasculature. Effective temporal resolution in fMRI, on the other hand, is limited by the hemodynamic response, which takes effect within roughly 1-2 seconds<sup>19</sup> (**Figure 1.4**).

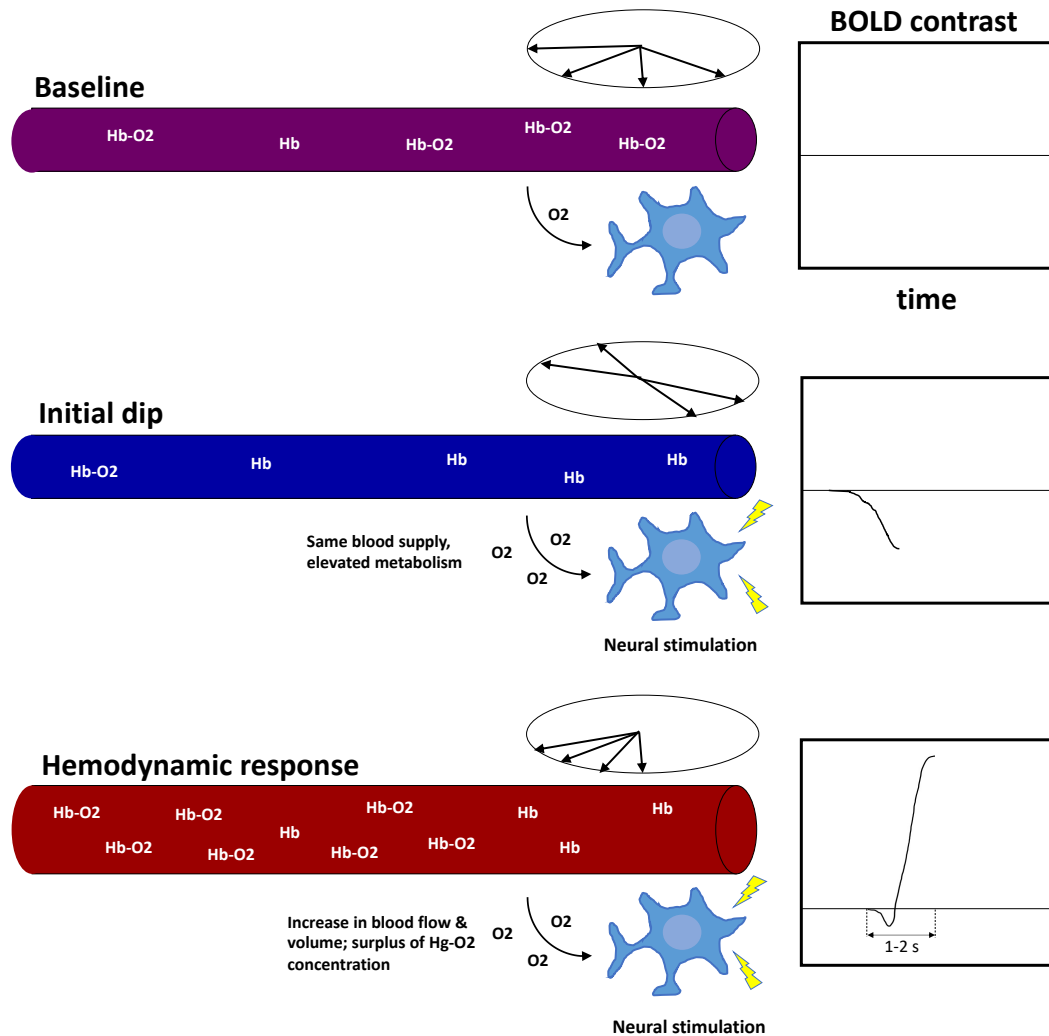


**Figure 1.4:** Schematic of the blood oxygenation level-dependent (BOLD) effect. At baseline, there is a moderate supply of oxygen (O<sub>2</sub>) to the neuron. Immediately following the start of neural stimulation, there is an increased O<sub>2</sub> demand for the neuron, resulting in a high concentration of deoxyhemoglobin (Hb) in the supplying capillary. Due to the susceptibility mismatch between strongly paramagnetic Hb and weakly diamagnetic blood vessels and brain tissue, the magnetic field near the stimulated neuron is weakened, as shown by the dephased spins. Shortly following this initial dip, there is an increase in blood volume and flow to the neuron in a process called the hemodynamic response. The result is concentrations of oxyhemoglobin (Hb-O<sub>2</sub>) and Hb that are greater than and less than at baseline, respectively, even after supplying O<sub>2</sub> to the neuron, and therefore an increased BOLD contrast.

## 1.2 Electroencephalography (EEG)

EEG is a direct measure of neural activity—*i.e.*, the extracellular electric potential generated by populations of neurons from ion fluxes in and out of cells. The EEG signal is sampled at a high rate—usually kilohertz. Most commonly, EEG refers to non-invasive measurement using recording electrodes placed on the scalp and will be referred to as such. This EEG signal suffers poor spatial resolution due to spatial smearing of the scalp potential distribution by the low-conductivity skull and poor SNR due to far recording distances and signal attenuation through the skull and meninges.

Ions constantly influx and efflux across cell membranes. These ion fluxes generate electric currents that, due to Ohm's law, cause an electric potential across the resistive cell membrane. A neuron's potential is modulated by inputs it receives from other neurons. Neurons are arranged in circuits and are connected by chemical synapses at their somas and dendrites. Inputs are in the form of neurotransmitters—chemicals released from the presynaptic neuron that cross the synaptic cleft and interact with receptors on the postsynaptic membrane. These postsynaptic receptors are responsible for opening or closing channel proteins specific to one or more ions. The transmission of ions across these channels modulates the postsynaptic neuron's potential. Hence, a neuron's potential is modulated by excitatory (EPSPs) and inhibitory postsynaptic potentials (IPSPs), which correspond to making the potential less or more negative—*i.e.*, depolarization and hyperpolarization, respectively<sup>51</sup>.

Generally, a single synapse is purely excitatory or inhibitory. The currents across the synaptic cleft of an excitatory synapse cause an active sink in the extracellular space near the synapse with passive sources along the rest of the soma-dendritic membrane.

Similarly, an active source is created at an inhibitory synapse with passive sinks along the rest of the membrane. Such source-sink configurations form effective electric dipoles that are responsible for extracellular potentials (**Figure 1.5B**)<sup>3</sup>.

The major contributor to the EEG signal is the extracellular potential generated by synchronously active cortical pyramidal neurons. Since these neurons are arranged in palisades with apical dendrites perpendicular to the cortical surface, they act as a dipole layer with electric potentials measurable as distant as the scalp (**Figure 1.5C**)<sup>3</sup>.

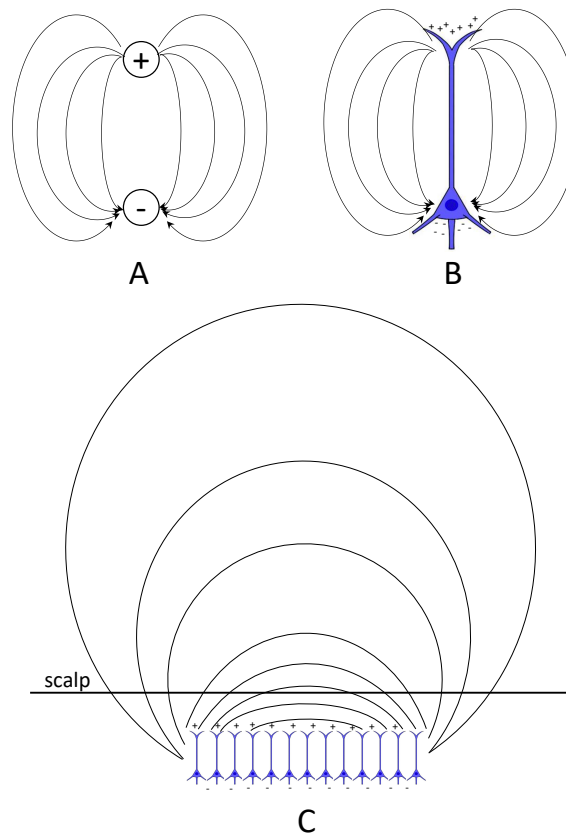


**Figure 1.5:** Dipoles formed by pyramidal neurons in generating the EEG signal. **(A)** An electric dipole is the set of one positive and one negative charge, and the current that flows between them. **(B)** Since cortical pyramidal neurons' postsynaptic inputs are either inhibitory or excitatory, the entire cell is roughly modeled as an electric dipole. **(C)** Cortical pyramidal neurons are commonly arranged in palisades and fire synchronously, making their net extracellular potential detectable as far as the scalp. (Neuron graphic courtesy of Marc Dingman of NeuroscientificallyChallenged.com. Proof of permission provided in Appendix A.)

The synchronized rhythmic firing of populations of neurons is responsible for the wave property where the EEG signal fluctuates over time. In different frequency bands, distinct patterns and properties have been observed. EEG waves exhibit a frequency distribution approximately following amplitude  $1/f$ , where  $f$  is the frequency. The classical EEG frequency bands are defined as: delta 1-4 Hz; theta 4-8 Hz; alpha 8-12 Hz; beta 12-30 Hz; and gamma above 30 Hz<sup>52</sup>.

An example of a band-specific phenomenon is alpha blocking. Alpha activity is in general mostly generated by posterior brain regions. In these posterior regions, alpha amplitudes decrease and beta amplitudes increase in response to the opening of the eyes. Alpha blocking is detectable at electrodes placed at posterior portions of the scalp<sup>52</sup>.

There are a number of shortcomings of EEG signal quality. Action potentials, also called spiking potentials, are usually not strong enough to be detected at the scalp. Moreover, since the EEG signal is from synchronous populations of neurons, nonsynchronous neurons do not contribute and cannot be studied<sup>53</sup>. The SNR in EEG is low due to the scalp being far from the cortical signal source and due to attenuation by the meninges and skull. This attenuation is especially impactful for higher frequencies and therefore the tissues act as a low-pass filter<sup>54</sup>. Lastly, spatial resolution is poor since the low conductivity of the skull smears the potential distribution on the scalp surface<sup>55</sup>.

Electrodes are placed on the scalp according to a standardized anatomic landmark-based system called the International 10-20 system. The name of this system comes from the fact that the distance between adjacent electrodes is 10% or 20% of the anteroposterior or lateral distances of the skull. Electrodes on the left and right halves of the skull are numbered odd and even, respectively, with electrodes along the midline

numbered zero ('z'). In the most basic configuration, 21 electrodes are arranged as in **Figure 1.6A**. Additional electrodes can be placed as in **Figure 1.6B**<sup>56</sup>.

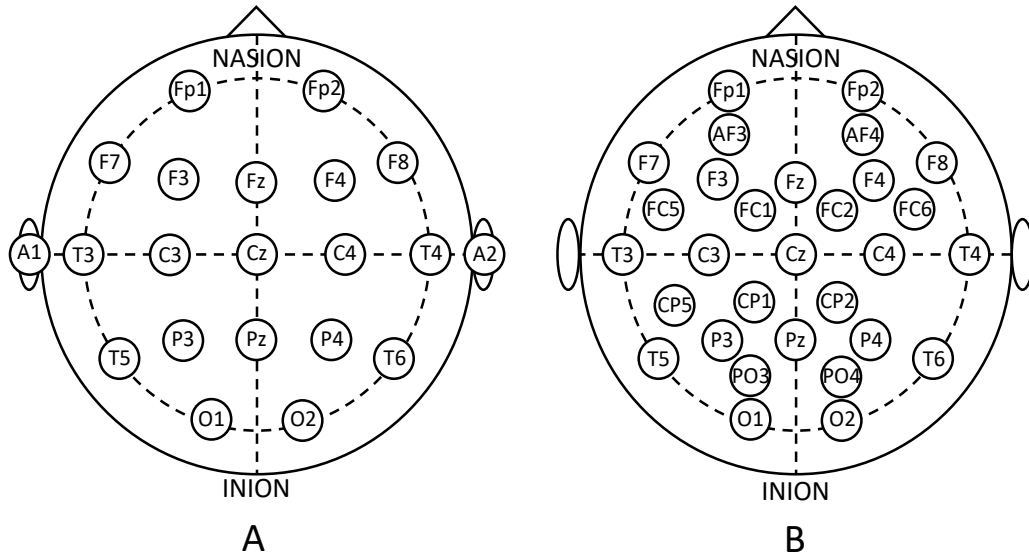


**Figure 1.6:** Examples of scalp electrode configurations. **(A)** The basic 21-electrode configuration. **(B)** A 30-electrode configuration. Fp, prefrontal; F, frontal; AF, between Fp and F; C, central; FC, between F and C; T, temporal; P, parietal; CP, between C and P; O, occipital; PO, between P and O; A, earlobe reference.

There are two main ways to electronically reference the electrodes. The first is bipolar recording, in which the EEG signals of the various scalp electrodes are referenced to one or more of these same scalp electrodes. The second is monopolar recording in which an extra electrode, presumed to be mostly free of brain activity, is used as the reference for all scalp electrodes. A common source of monopolar reference is one or both earlobes<sup>56</sup>.

Since the EEG signal at a single electrode is a weighted sum of multiple sources, it is impossible to identify with full certainty the intracerebral sources of each electrode's signal. This is an inverse problem with no unique solution. Estimation of the intracerebral

sources of each electrode's signal also requires an accurate model of the geometry and conductivities of the various tissues in the head. Estimates are usually computed by minimizing an error metric between the recorded signal and the simulated signal from a given combination of intracerebral sources<sup>12</sup>. Common models of intracerebral EEG generators are an equivalent dipole, an anatomic prior-based model, and low-resolution electromagnetic tomography (LORETA), the latter of which is based on the assumption that synchronously and simultaneously active brain regions are most likely neighbours<sup>57</sup>.

### **1.3 Simultaneous EEG and fMRI (EEG-fMRI)**

EEG and fMRI have been acquired simultaneously for over two decades<sup>7,9,58–61</sup> due to their complementary strengths. EEG measures neural activity directly using electrodes sensitive to voltages induced by ion fluxes during action potentials and postsynaptic potentials<sup>62</sup>. EEG is generally recorded at a high sampling rate, on the order of kilohertz. However, EEG has poor spatial resolution due to the low conductivity of the skull smearing the potential distribution over the scalp surface<sup>55</sup>. In fMRI, a timeseries of images is acquired. Voxels are on the scale of hundreds of microns to millimeters, and each voxel's intensity provides a spatially specific measure of the concentration of local deoxygenated hemoglobin—an endogenous paramagnetic contrast agent<sup>14</sup>. Since the concentration of deoxygenated hemoglobin correlates with neural activity through hemodynamic processes, fMRI is an indirect measure of neural activity. The hemodynamic response is on the order of a couple of seconds, giving fMRI poor temporal resolution regardless of how fast each image is acquired. Thus, the high temporal resolution and low spatial resolution of EEG complements the high spatial

resolution and low temporal resolution of fMRI.

### **1.3.1 fMRI artifacts in EEG-fMRI**

High-quality MRI relies on the homogeneity of the main static magnetic field. Magnetic field homogeneity is compromised at material interfaces since the local magnetic field depends on the change in the material-specific property known as magnetic susceptibility. At the high fields used in MRI, even small differences in magnetic susceptibility can manifest as signal dropout, geometric distortion, and sometimes image ghosting. Therefore, the presence of electrode caps—which contain electrodes typically made of Ag/AgCl, resistors, copper wires, and conductive gel—has been found to impart artifact in images. Given that most of the materials used (with the exception of safety resistors) for EEG recording acquired in the MRI scanner are weakly diamagnetic just like tissue, these artifacts are often minor<sup>63</sup>.

The RF field used in MRI to excite the sample is also subject to unwanted inhomogeneities. In a conductive or dielectric material, such as the electrodes (including wires) and head, respectively, the RF field is altered as a result of induced surface currents that act to shield the object from the field. Therefore, the electrodes contribute to an inhomogeneous RF field profile of the head. This results in images with signal dropouts and geometric distortions. Correction of RF field-related inhomogeneities is an area of active research<sup>63</sup>.

### **1.3.2 EEG artifacts in EEG-fMRI**

Artifacts in the EEG data are induced voltages  $\mathcal{E}$ . Faraday's law states that  $\mathcal{E}$  arises from a time-varying magnetic flux  $\Phi$  through a closed conductive loop. Consider the following

form of Faraday's law for a spatially uniform magnetic field:

$$\mathcal{E} = -\frac{d\Phi}{dt} = -\frac{d}{dt}(\vec{B} \cdot \vec{A}) = -\frac{d}{dt}(BA \cos \theta), \quad (1.3.1)$$

where  $\vec{B}$  is the magnetic field,  $\vec{A} = A\hat{n}$  is the surface formed by the loop with normal vector  $\hat{n}$ , and  $\theta$  is the angle between  $\vec{B}$  and  $\hat{n}$ . In the case of EEG-fMRI, a closed conductive loop is formed through the EEG amplifier, electrodes and cables, and tissue<sup>64</sup>. In practice, one must account for the spatial non-uniformity of the magnetic field when applying Faraday's law. However, Equation 1.3.1 serves as a useful illustration of the variables involved in generating the gradient artifact.

Efforts have been made to reduce  $\mathcal{E}$  by minimizing  $\vec{A}$ —*i.e.*, twisting the wires together as much as possible. As is apparent from Equation 1.3.1,  $\mathcal{E}$  can arise from a time variation in any or all of  $\vec{B}$ ,  $\vec{A}$ , and  $\theta$ . Movement of the electrode leads during scanning, which arises from ballistocardiograms, head movement, and scanner vibration, is responsible for time variation in  $\vec{A}$  and  $\theta$  and, therefore, is a source of artifact. Electrode motion is minimized by restraining the various parts of the EEG apparatus, such as by immobilizing the electrodes in a skull cap (**Figure 1.7A**) and weighing down the cables<sup>65</sup>.

$\vec{B}$  changes in time as a result of (1) one's cardiac pulse modulating the local static field near blood vessels and (2) the RF and gradient pulses applied during imaging. The pulse artifact, also known as the ballistocardiogram artifact, overlaps with the EEG signal in time and frequency and commonly has an amplitude comparable to or greater than the EEG signal. The pulse artifact is found to have a repetition frequency and phase roughly the same as the pulse in one's corresponding electrocardiogram (ECG), as well as a similar shape. The shape over time, however, varies considerably. Processing methods

for pulse artifact removal include AAS, the temporal principal component analysis (temporal PCA)-based optimal basis set method (OBS), Kalman filtering, wavelet transformation and nonlinear noise reduction, a moving general linear model, spatial PCA, and spatial independent component analysis (spatial ICA)<sup>66</sup>. Since AAS, OBS, and spatial ICA are also used for gradient artifact removal, they are explained in Section 1.4.2.

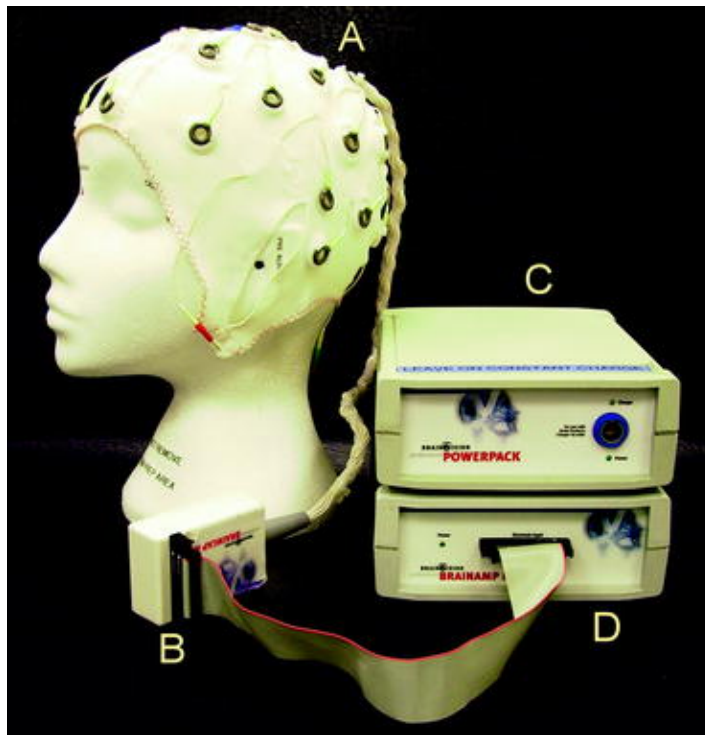


**Figure 1.7:** A common EEG-fMRI recording apparatus. (A) A skull cap is used to restrain the electrode leads from head motion, ballistocardiographic motion, and scanner-related vibrations. The electrode wires are twisted together to further minimize motion as well as current loop area. (B) a designated box containing current-limiting resistors. (C) A wireless battery for the amplifier. (D) A multi-channel amplifier-digitiser unit. (Reprint of Figure 1 of EEG Instrumentation and Safety by Phillip J. Allen by permission from Springer, Berlin, Heidelberg; copyright 2019; licence agreement found in Appendix A.)

The RF and gradient pulses applied during imaging are time-varying magnetic fields that impart artifact to the EEG data as per Faraday's law. The amplitudes of the RF

and gradient artifacts are several of orders of magnitude greater than that of the EEG signal and, by definition, overlap in time with simultaneously acquired EEG data, thereby necessitating their removal. The RF artifact's fundamental and largest-magnitude frequency component is at the Larmor frequency, which is on the order of megahertz and is not of concern as it is easily low-pass-filtered from the EEG signal, which does not exceed 200 Hz. Some RF artifact also manifests at the frequency of repetition of the RF pulse, which is typically below 1 Hz in accordance with the fMRI volume repetition time and is removed by high-pass filtering<sup>67</sup>. The gradient artifact—the removal of which is the subject of this thesis—is the most detrimental artifact in EEG-fMRI and is presented in the following sub-chapter.

## 1.4 The gradient artifact

The gradient artifact overlaps with the EEG signal in frequency as well as time, having a fundamental component at the frequency of slice acquisition—commonly around 10 Hz—as well as harmonics that can extend into the kilohertz range. Since the gradient artifact overlaps in both frequency and time with the EEG signal, and since it exceeds it by one to three orders of magnitude, it is the dominant artifact in the EEG data<sup>21–24</sup> and hampers analysis<sup>22,68</sup> (**Figure 1.8**).

### 1.4.1 Gradient artifact structure

Recall that the EEG artifact depends on the time-variation in the magnetic field, the current loop area, and the relative angle between the loop and the field. If the values of all these variables were known at an electrode over all times of EEG-fMRI recording, the

exact gradient artifact waveform could be known at that channel. Furthermore, since the combination of these variables' values differ across the different electrodes, the various electrode channels exhibit different albeit similar gradient waveforms. Due to the common pulse sequence experienced at each electrode, the timings of the slews in the gradient artifacts are the same across channels<sup>64</sup> (**Figure 1.9**).

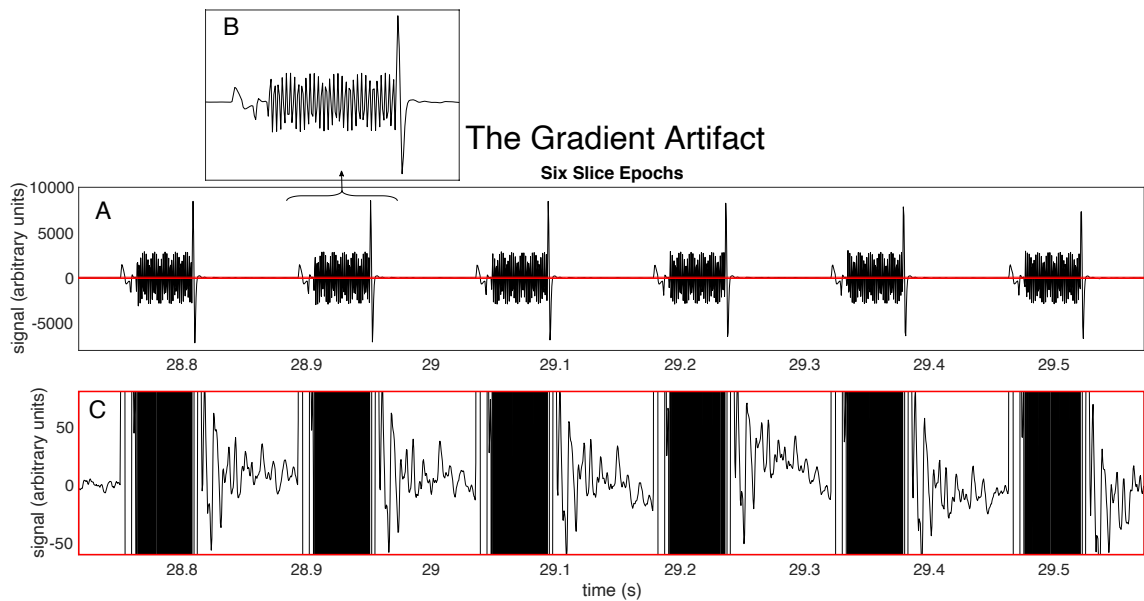


**Figure 1.8:** The gradient artifact.

(A) Six slice epochs that contain gradient artifact. At full vertical scale, the EEG is unresolvable in relation to the large-amplitude artifact. (B) A temporal closeup of the gradient artifact from a single slice epoch. The shape of the artifact follows from the different gradient pulses applied. (C) A vertical closeup of the EEG signal from the slice epochs. On this amplified vertical scale, the EEG signal is resolvable.

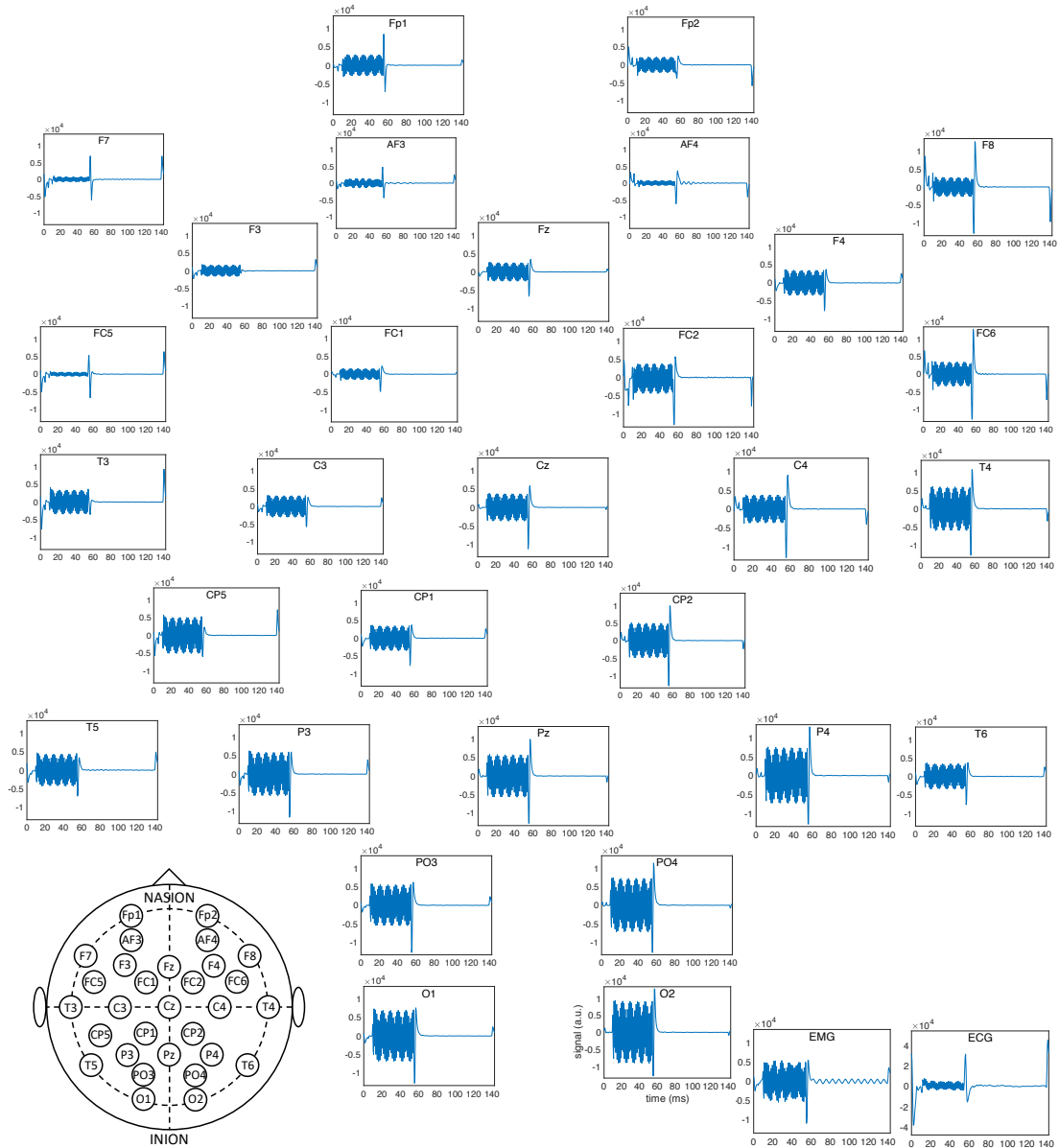


**Figure 1.9:** Variation of the gradient artifact across channels.

The first raw slice acquisition epoch, as defined by the triggers, is shown for each channel. Fp, pre-frontal; F, frontal; AF, between Fp and F; C, central; FC, between F and C; T, temporal; P, parietal; CP, between C and P; O, occipital; PO, between P and O; EMG, electromyography.

## **1.4.2 Gradient artifact removal methods**

### **1.4.2.1 Interleaved acquisition**

Interleaved acquisition of EEG between image slices does not technically qualify as simultaneous acquisition of EEG and fMRI but has been used to avoid the gradient artifact<sup>9,35–38,58,69–74</sup>. This approach disrupts the temporal continuity of the signal and promotes compensation in the form of a longer repetition time (and therefore poorer temporal resolution) and shortened gradient pulses, the latter of which is potentially constrained by limits on slew rate, gradient amplitude, and specific absorption rate.

### **1.4.2.2 Stepping-stone sampling**

Stepping-stone sampling is a contrived setup for EEG-fMRI where EEG is sampled exclusively between gradient pulses while the gradients are at baseline<sup>21</sup>. Stepping-stone sampling requires synchronization of the EEG and MRI clocks, as well as a special MRI pulse sequence. Stepping-stone sampling is able to markedly reduce the raw gradient artifact.

### **1.4.2.3 Low-pass filtering (LPF)**

Low-pass filtering (LPF) in the frequency domain using a cutoff frequency at the upper end of the EEG band has also been used to reduce the gradient artifact<sup>21–23,40</sup>. However, the frequency profile of the gradient artifact is dominated by peaks corresponding to the slice frequency—the number of slices per volume divided by the volume repetition time—and its harmonics, which overlap with the EEG frequency band. LPF is therefore unable to remove much of the gradient artifact.

#### **1.4.2.4 Notch filtering**

Notch filtering—*i.e.*, zeroing or reducing the weight of the Fourier components corresponding to the slice frequency and its harmonics—has been proposed<sup>25,26</sup>. This carries the disadvantages of completely or mostly removing EEG signal at these frequencies, as well as producing a ringing artifact.

#### **1.4.2.5 Reference layer artifact subtraction**

Dedicated EEG caps have been manufactured that have an extra reference layer of electrodes in contact with tissue-like material—*i.e.*, agar or physiological saline<sup>27,28</sup>. The reference signals provide a simultaneous, non-neural, artifact-only version of that recorded from the scalp electrodes. Subtraction of the reference signals from their respective scalp signals has been shown to remove much of the gradient artifact, albeit not all of it, without disrupting the EEG signal. Implementation is difficult, however, as no such electrode cap is currently on the market. Moreover, this method does not apply to studies of intra-cranial EEG. Hence, post-acquisition processing is favoured.

#### **1.4.2.6 Average artifact subtraction (AAS)**

To date, the most accepted post-acquisition processing step is AAS<sup>22</sup>, which locally averages the artifact-containing signal using temporal units of slice epochs, as defined by scanner triggers, so as to form a template of the artifact that is subtracted from the signal. AAS takes advantage of the weakly stationary gradient artifact, which occurs once per slice acquisition and has a roughly constant phase, frequency profile, and amplitude profile. EEG signal, however, is uncorrelated from one slice epoch to another. The average slice epoch, therefore, qualifies as an artifact template since its artifact component is nearly identical to that of the individual slice epochs while its neural

content mostly cancels. Subtraction of such a template from each slice epoch has been shown to dramatically reduce gradient artifact. Potential major practical limitations of AAS are (i) artifact phase jitter caused by asynchrony between the sampling clocks of the EEG recorder and MRI scanner, (ii) artifact amplitude jitter caused by motion of the electrodes during acquisition, and (iii) persistence of neural content in the artifact template due to significant correlation of neural signal between slice epochs. Several techniques have been devised for remedying these limitations.

(i) A common issue with EEG data acquired during fMRI is that the sampling clocks of the EEG acquisition unit and MRI scanner are out of phase. This results in the timing of the gradient pulse being out of phase with the EEG sampling, resulting in phase jitter of the gradient artifact. Artifact phase jitter severely limits the effectiveness of AAS since the artifact template poorly represents the individual artifact per slice (**Figure 1.10**). Several post-acquisition techniques have been devised to ameliorate artifact phase jitter, such as interpolation, followed by phase-shifting the slice epochs<sup>8,23,75</sup>. One highly effective prospective technique to nearly or entirely prevent artifact phase jitter is the use of supplementary electronics that synchronize the clocks of the EEG and MRI<sup>24</sup>. The success of these electronics requires that the sampling rates of the fMRI slice acquisition and EEG are integer multiples of one another. Moreover, the compatibility of such a commercial product<sup>76</sup> ([brainproducts.com/productdetails.php?id=19](http://brainproducts.com/productdetails.php?id=19)) is only certified in Philips scanner systems. Thus, there are significant barriers to preventing artifact phase jitter.

(ii & iii) Returning to Faraday's law, the induced voltage depends on the angle between the magnetic field and the conductive loop. Electrode motion changes this angle,

thereby modulating the artifact amplitude and limiting the effectiveness of AAS. To account for changes in artifact amplitude, EEG data is usually binned according to some metric of similarity, such as temporal localness, and AAS is performed per bin<sup>8</sup>. EEG activity is not necessarily significantly uncorrelated between slice epochs. Such an assumption bears the risk of losing EEG information by incorporating EEG activity in the artifact template, which gets subtracted. Epoch censoring during template formation is sometimes done for epochs that show anomalous structure—*e.g.*, due to templates containing significant amounts of EEG or motion—thereby minimizing signal loss<sup>22,23,30,38,77</sup>.

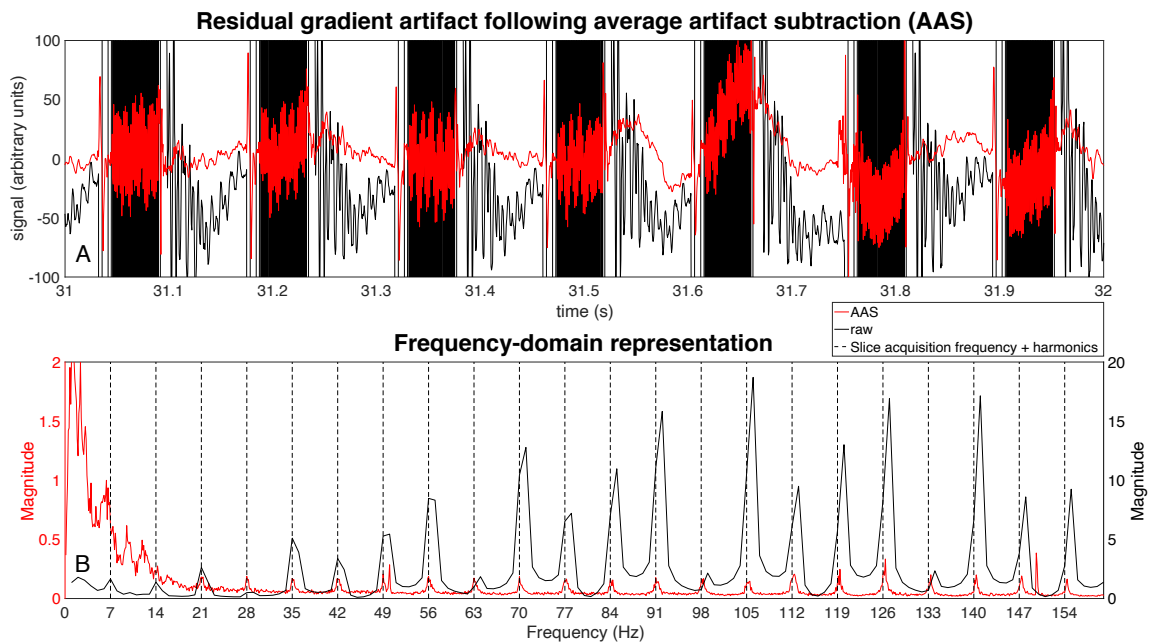


**Figure 1.10:** Residual gradient artifact following AAS. **(A)** In the time domain, the residual artifact is clearly present based on the difference in amplitude between times during which the gradients are on and off. **(B)** In the frequency domain, gradient artifact spikes in the FFT magnitude occur roughly every 7 Hz, which corresponds to the fundamental slice acquisition frequency (21 slices / 3-second volume TR) and harmonics. These spikes are present in both the raw (black) and post-AAS (red) data, displayed with different scales. (The raw and AAS spectra were binned and averaged every 1 and 0.125 Hz, respectively.)

#### **1.4.2.7 Temporal PCA/Optimal basis set (OBS)**

Temporal PCA has been applied to the data following AAS. Temporal PCA forms a set of orthogonal basis functions—or principal components—of a timeseries. Assuming the residual artifact contains the most variance of the residual artifact-containing data, the first few principal components, which capture the most signal variance, are declared the OBS and are added to the artifact template from AAS. The improved template is subtracted from the pre-AAS data<sup>23</sup>. Alternatively, EEG data acquired in the absence of scanning has been used as a reference to which all principal components of the residual-containing data are weighted<sup>32</sup>.

#### **1.4.2.8 Adaptive noise cancelation (ANC)**

Adaptive noise cancellation (ANC) is a technique that filters an input signal corrupted with noise or artifact until its residual with a reference signal is minimized<sup>78</sup>. The reference signal is an estimate of the pure noise or artifact. ANC has been used to reduce the residual artifact following AAS. Some reference signals used are a binary comb equal to 1 at the slice timings<sup>22</sup> and the estimated artifact template following temporal PCA<sup>23</sup>.

#### **1.4.2.9 Spatial independent component analysis (spatial ICA)**

ICA is a technique that, given multiple inputs, outputs independent components (ICs) that represent statistically independent sources of the inputs<sup>79</sup>. Spatial ICA—ICA with multiple inputs in space—is attractive for gradient artifact removal because these artifacts are statistically independent from the EEG signal and vary structurally over space, and because it is insensitive to phase jitter<sup>26,33,34,40</sup>. However, spatial ICA is limited by the number of ICs, which is limited by the number of recording channels. This reduces its ability to accurately separate between signal and artifact. A further drawback of spatial

ICA is that usually, the user must be involved in some capacity in judging which ICs contain a significant amount of artifact.

## 1.5 Schrödinger filtering

Although processing steps following AAS reduce the residual gradient artifact, satisfactory artifact removal and EEG preservation across all frequency bands remains elusive<sup>41</sup>. We present a pipeline that removes gradient artifact and preserves EEG signal without compromise across all frequency bands up to the upper-gamma band (120 Hz). The pipeline only includes AAS followed by the proposed Schrödinger filtering technique. Schrödinger filtering is based on semi-classical signal analysis (SCSA)<sup>42</sup>, which employs the discrete spectrum of the Schrödinger operator. An input signal, treated as an attractive potential in the Schrödinger operator, is decomposed into a set of weighted squared eigenfunctions called Schrödinger components. Schrödinger components are pulse-shaped signals that individually describe one or more peaks of the input signal. Schrödinger components have distinct energies ranging from high to low. SCSA reconstructs the input signal using the Schrödinger components, and is therefore analogous to the discrete Fourier transform, which reconstructs a signal with a set of sinusoids of varying frequency. Schrödinger filtering generates components that separately capture signal and artifact based on energy differences in a manner analogous to frequency-domain bandpass filtering, and preserves the EEG signal, which overlaps in time and frequency with that of the gradient artifact.

### 1.5.1 Semi-classical signal analysis (SCSA)

It is common to analyze a timeseries according to its frequencies using the discrete Fourier transform. The analysis of a pulse-shaped timeseries according to its energies, on the other hand, is a new technique called semi-classical signal analysis (SCSA)<sup>42</sup>. In SCSA, a pulse-shaped input signal is treated as an attractive potential in the one-dimensional Schrödinger operator. The discrete spectrum of the Schrödinger operator, corresponding to a discrete set of energies of the signal, is used to analyze the signal.

The Schrödinger equation was conceived for analysis of quantum-mechanical systems in which a particle follows some trajectory over space and time in the presence of some external force. The Schrödinger equation is used to calculate the system's wave function, which allows one to determine the probability of measuring the particle in a certain region of space at a certain time<sup>80</sup>. SCSA utilizes the simplest form of the Schrödinger equation—*i.e.*, the one-dimensional, time-independent form—in which the particle moves in one dimension  $x$  and is subject to an external force that does not explicitly depend on time. The one-dimensional, time-independent Schrödinger equation is therefore expressed only in terms of  $x$  and not in terms of time. However, in SCSA,  $x$  is replaced by the variable  $t$  to more intuitively denote the independent variable of the input timeseries. The variable  $t$  should therefore not be confused with time as it applies in quantum mechanics.

In the general signal processing context motivated thus far, the Schrödinger equation is introduced as an eigenvalue problem:

$$H_h(t)\psi(t) = \lambda\psi(t), \quad (1.5.1)$$

where  $H_h(t)$  is the Schrödinger operator,  $\psi(t)$  is an eigenfunction on which  $H_h(t)$

operates, and  $\lambda$  is an eigenvalue. The Schrödinger operator  $H_h(t)$  is

$$H_h(t) = -h^2 \frac{d^2}{dt^2} - s(t), \quad t \in \mathbb{R} \quad (1.5.2)$$

where  $h \in \mathbb{R}_{>0}$  is known as the semi-classical parameter and  $s(t) \in \mathbb{R}_{\geq 0}$  is a one-dimensional input signal. (Note the requirement that  $s(t)$  is nonnegative. In practice, signals not purely nonnegative are subtracted of their minima in order to allow for processing by SCSA.) The value of  $h$  is crucial in SCSA's ability to represent  $s(t)$ , which, as will be made clear, is optimal in the semi-classical limit of  $h \rightarrow 0$ .

There is a finite spectrum of eigenvalues that can be organized into two parts: a continuum of positive eigenvalues  $\lambda > 0$  plus a discrete spectrum of negative eigenvalues  $\lambda = -\kappa_{h,n}^2; \kappa_{h,n} > 0; n = 1, 2, \dots, N_h$ . Deift and Trubowitz<sup>81</sup> showed that if  $s(t)$  at least weakly satisfies three conditions, it can be expressed as

$$s(t) = \frac{2i}{\pi} \int_{-\infty}^{+\infty} kR(k)f^2(t, k)dk + 4 \sum_{n=1}^{N_h} \kappa_{h,n} \psi_{h,n}^2, \quad (1.5.3)$$

where  $k = \frac{2\pi}{t}$ ,  $R(k)$  is the so-called reflection coefficient, the name of which originated from quantum scattering, and  $f(t, k)$  is the solution corresponding to the continuous spectrum. The conditions are:

- (I)  $s(t)$  must be infinitely differentiable to ensure it is smooth and continuous;
- (II)  $s(t)$  must asymptotically go to zero quickly according to

$$\int_{-\infty}^{+\infty} |s(t)|(1 + |t|)dt < \infty; \text{ and}$$

- (III)  $-s(t)$  must be attractive. *I.e.*,  $s(t) \geq 0$ .

There is a special class of potentials called reflectionless potentials for which  $R = 0$ , and, consequently, the first term on the right-hand side of Equation 1.5.3 is zero.

Therefore, reflectionless potentials may be expressed exclusively in terms of the eigenvalues and eigenfunctions from the Schrödinger equation (Equation 1.5.1):

$$s(t) = 4 \sum_{n=1}^{N_h} \kappa_{h,n} \psi_{h,n}^2. \quad (1.5.4)$$

One example of a reflectionless potential is the soliton<sup>82</sup>: a traveling wave packet that maintains its shape while moving at a constant speed. If  $s(t)$  is a soliton or multiple solitons in interaction traveling in the  $t$ -dimension, the individual terms in the series of Equation 1.5.4 are solitons or multi-solitons as well.

The goal of SCSA is to reconstruct an input signal  $s(t)$  using the discrete spectrum of  $H_h(t)$ . For reflectionless potentials, this goal is achieved with Equation 1.5.4. Most input signals are not reflectionless, however. Laleg-Kirati et al.<sup>42,83</sup> showed that input signals  $s(t)$  satisfying conditions (I)-(III) are reconstructed as with the discrete spectrum of  $H_h(t)$  in the semi-classical limit of  $h \rightarrow 0$ :

$$\tilde{s}_h(t) = 4h \sum_{n=1}^{N_h} \kappa_{h,n} \psi_{h,n}^2(t), \quad t \in \mathbb{R}, \quad (1.5.5)$$

where  $\tilde{s}_h(t)$  is the output signal. Note that Equation 1.5.5 is equivalent to Equation 1.5.4 except for the incorporation of the  $h$  parameter. Each term  $4h\kappa_{h,i}\psi_{h,i}^2(t)$  is referred to as a Schrödinger component (**Figure 1.11**).

Starting with a high  $h$ -value, few Schrödinger components  $N_h$ , characterized by their high energies, are produced in the Schrödinger series according to Equation 1.5.5. A Schrödinger series with a small value of  $N_h$  broadly reproduces the shape of  $s(t)$  without fully reconstructing it (**Figure 1.11A**). By decreasing  $h$ , however, more components are generated in the series (**Figure 1.11B**). The higher-order, lower-energy components

capture the fine details of  $s(t)$ , allowing for full signal reconstruction (**Figure 1.11C**). Indeed, for a continuous—*i.e.*, not discrete—signal,  $s(t)$  is perfectly reconstructed in the semi-classical limit of  $h$  tending to zero<sup>42</sup>. However, for discrete signals, this limit breaks down below some critical  $h$ -value, called  $h^*$ , due to sampling inadequacies. Thus, for a discrete  $s(t)$ , optimal approximation by SCSA is achieved for  $h = h^*$  and consequently  $N_h = N_h^*$ , where  $h^*$  is defined as the root of the minimum of the mean squared error  $J(h)$ :

$$J(h) = \frac{1}{M} \sum_{m=1}^M (s(t) - \tilde{s}_h(t))^2; \quad (1.5.6a)$$

$$J(h^*) = \min(J(h)). \quad (1.5.6b)$$

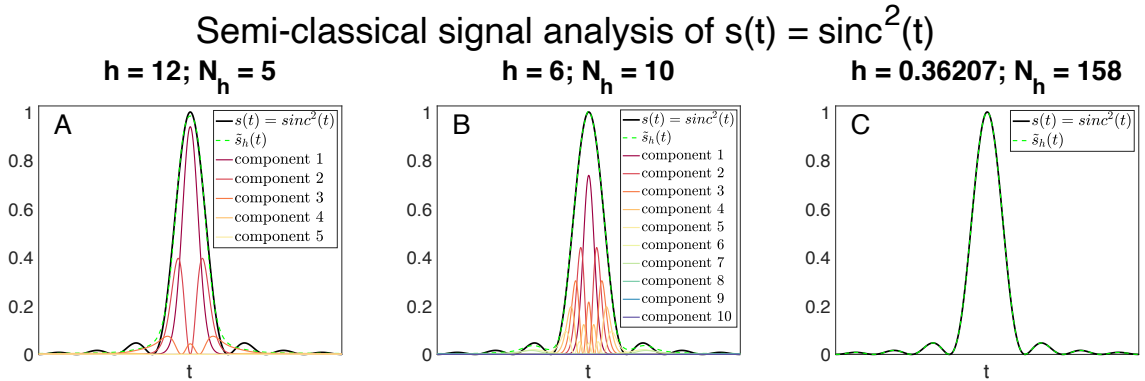


**Figure 1.11:** Illustration of SCSA.

The Schrödinger components generated by SCSA are nonnegative pulse-like signals that sum to the nonnegative input signal. Earlier components are higher-energy and depict the largest peaks in the input signal. A simple example is given in which the squared cardinal sine function  $s(t) = \text{sinc}^2 t$  is reconstructed by SCSA. **(A)** With the relatively high  $h$ -value of  $h = 12$ , there is a low number of components ( $N_h = 12$ ) and the signal is under-constructed. **(B)** When a smaller  $h$ -value ( $h = 6$ ) is used, there is a greater number of components ( $N_h = 10$ ) and the input signal is better represented but is still appreciably deviant. **(C)** With a much smaller  $h$ -value ( $h = 0.36207$ ), the input signal is fully constructed with  $N_h = 158$  components.

SCSA’s ability to represent  $s(t)$  as a sum of energy-based components offers flexibility and utility in data-cleaning applications. For example, the Schrödinger series of a blood pressure signal has been used to separate between the systolic and diastolic components<sup>42</sup>; selection of  $N_h < N_h^*$  has been used for denoising of magnetic resonance imaging (MRI) and magnetic resonance spectroscopy (MRS) data<sup>84,85</sup>; and water peak suppression in proton MRS data by exclusion of low-order Schrödinger components has been found to be effective<sup>86</sup>. In the present work, we exploit SCSA to separate the residual gradient artifact from the EEG signal in a process named Schrödinger filtering.

## 1.5.2 Schrödinger filtering

Whereas SCSA is the representation of a signal with a Schrödinger series, Schrödinger filtering is the adaptation of SCSA to remove residual gradient artifact from the post-AAS time-domain data  $y_{aas}(t)$ . Schrödinger filtering consists of two steps—de-spiking and global filtering—each of which adapts SCSA differently. First, de-spiking is applied on  $y_{aas}(t)$  to remove large gradient-related spikes that were not significantly attenuated by AAS. This is done by subtracting high-energy Schrödinger components that correspond to spikes. De-spiking is valuable for the next step of global filtering as it allows for a finer separation between artifact and signal. The resultant de-spiked signal  $y_{ds}(t)$  is then processed by global filtering to accurately extract the EEG signal  $y_{sf}(t)$ . Global filtering entails reconstruction of  $y_{ds}(t)$  using  $N_h < N_h^*$  so as to omit residual gradient artifact.

### 1.5.2.1 Step 1: de-spiking

Early components in the Schrödinger series of Equation 1.5.5 often solely depict large

positive spikes in a signal due to their high energy<sup>86</sup>. Positive and negative spikes are defined here as large peaks above or below the baseline of signal fluctuation, respectively. Primary components  $y_I(t)$  are such components that feature a single potential well-shaped function localized at the spike maximum. Secondary components  $y_{II}(t)$  are such components that are forktail-shaped and feature a pair of wells on either side of the spike (**Figure 1.12C**). Although there are components subsequent to  $y_{II}(t)$  with increasingly greater numbers of wells that depict a positive spike, they are also increasingly wide and low-amplitude. Therefore, using only  $y_I(t)$  and  $y_{II}(t)$  sufficiently captures the spikes and prevents EEG signal loss during de-spiking.

Since Schrödinger components are purely nonnegative, they are unable to solely depict the negative spikes in  $y_{aas}(t)$ . For optimal de-spiking of these negative spikes, the input signal must be vertically reflected. The complete de-spiking of  $y_{aas}(t)$  is therefore segmented into two parts: (1) positive de-spiking, where  $y_{aas}(t)$  is input to remove the positive spikes to yield  $y_{ds+}(t)$ ; and (2) negative de-spiking, where the vertical reflection of  $y_{ds+}(t)$  is input to subtract the negative spikes.

De-spiking of  $y_{aas}(t)$  is a subtraction of  $y_I(t)$  and  $y_{II}(t)$  with respective weights  $\beta_1$  and  $\beta_2$ . The values of  $\beta_1$  and  $\beta_2$  are such that the amplitude of the positive spike region is reduced to that of its neighbourhood (**Figure 1.12E**). The de-spiked signal  $y_{ds+}(t)$  (**Figure 1.12F**) is therefore

$$y_{ds+}(t) = y_{aas}(t) - \beta_1 y_I(t) - \beta_2 y_{II}(t). \quad (1.5.7)$$

Negative de-spiking is performed in the same manner as positive de-spiking but with an input of the negative of  $y_{ds+}(t)$  and new resultant  $y_I(t)$  and  $y_{II}(t)$  components (**Figure 1.12G**). The output, after reflecting back to the original orientation, is the fully de-spiked

signal  $y_{ds}(t)$  (**Figure 1.12H**).

In removing the gradient-related spikes, the timeseries is rid of amplitude-wise outliers without obliterating EEG signal. As a result, the next step of global filtering is markedly improved as it is able to more finely delineate gradient artifact from EEG signal.

### 1.5.2.2 Step 2: global filtering

Global filtering is applied on  $y_{ds}(t)$  to remove residual gradient artifact while preserving EEG signal. There is an optimal value of  $h = h^{sf} > h^*$  and, consequently,  $N_h = N_h^{sf} < N_h^*$  in the Schrödinger series of  $y_{ds}(t)$  for global filtering. The pair of  $(h^{sf}, N_h^{sf})$  is determined by minimizing the error between the portions of  $y_{ds}(t)$  during which the gradients were on and off during scanning (*i.e.*, during non-contiguous intervals  $T_{on}$  and  $T_{off}$ , respectively). The rationale for this error minimization is as follows. During  $T_{off}$ , there is presumably little to no gradient artifact present in  $y_{ds}$ . Moreover, since the data during  $T_{on}$  and  $T_{off}$  are temporally proximal, their EEG activity is similar (**Figure 1.12IJ**). Therefore,  $y_{ds}(t)$  during  $T_{off}$  is an accurate reference for  $y_{ds}(t)$  during  $T_{on}$ , allowing for effective estimation of  $(h^{sf}, N_h^{sf})$ .

Error minimization is conveniently performed in the frequency domain:

$$\Delta(N_h) = \frac{1}{F} \sum_f \left( \tilde{Y}_{ds,on}(f, N_h) - Y_{ds,off}(f) \right)^2; \quad (1.5.8a)$$

$$\Delta(N_h^{sf}) = \min(\Delta(N_h)), \quad (1.5.8b)$$

where  $\Delta(N_h)$  is the mean squared error as a function of  $N_h$ ;  $f$  is the frequency;  $F$  is the spectral bandwidth;  $\tilde{Y}_{ds,on}(f, N_h)$  is the magnitude spectrum of  $\tilde{y}_{ds}(t)$  during  $T_{on}$  for

$N_h$ ; and  $Y_{ds,off}(f)$  is the magnitude spectrum of  $y_{ds}(t)$  during  $T_{off}$  (Figure 1.12KLM).

Once  $(h^{sf}, N_h^{sf})$  are determined, the artifact-free signal  $y_{sf}(t)$  is constructed using

Equation 1.5.5 with  $h = h^{sf}$  and  $\tilde{y}_{ds}(t)$  as the input signal (Figure 1.12NO).

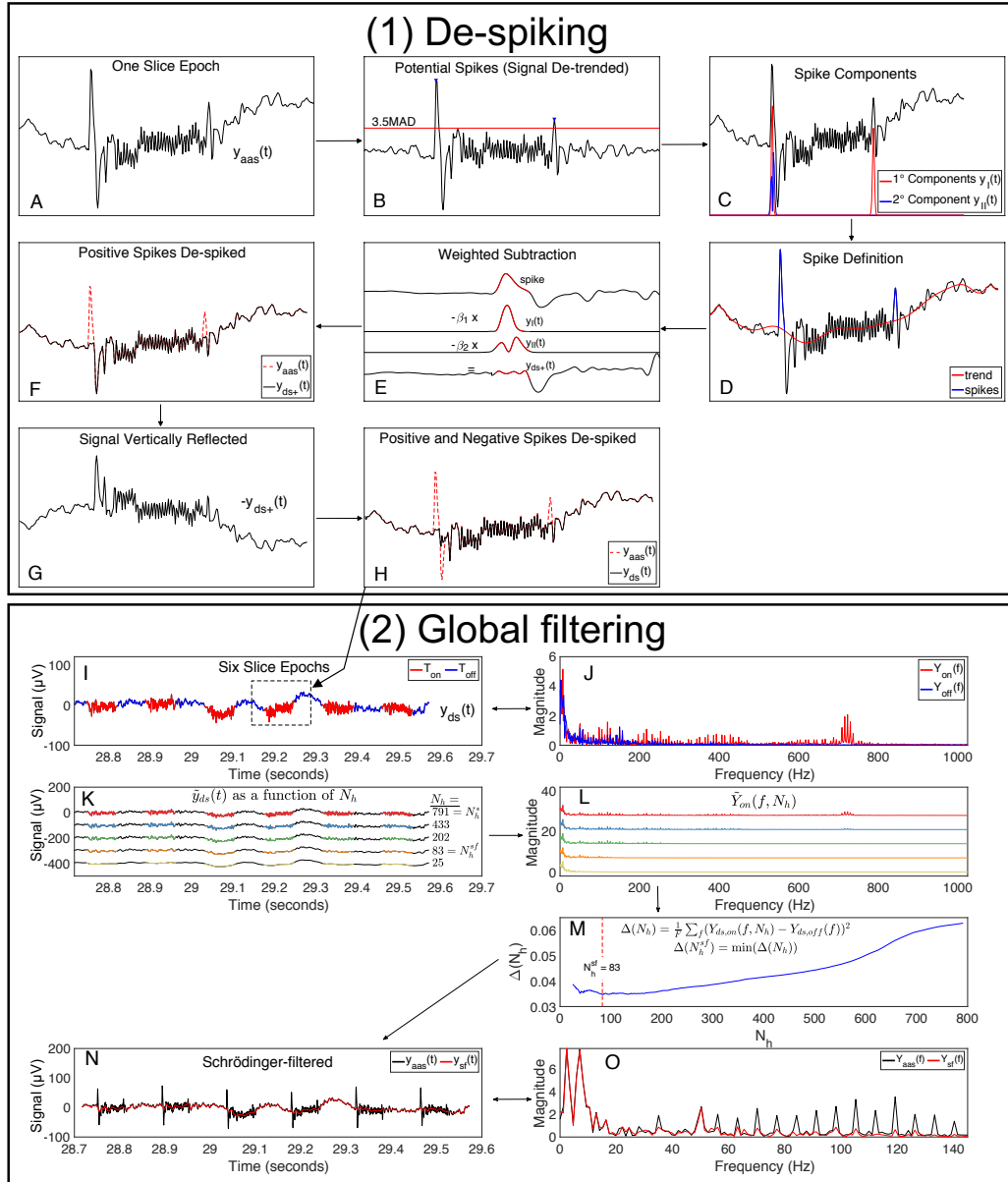


**Figure 1.12:** The Schrödinger filtering algorithm.

**(1) De-spiking:** To find the positive spikes,  $y_{aas}(t)$  (A) is de-trended and thresholded at 3.5 times the mean absolute deviation (MAD) (B). The peaks above the threshold that have a primary component  $y_I(t)$  (and sometimes a secondary component  $y_{II}(t)$ ) (C) are deemed positive spikes. After defining the ends of the spike using the

trend of the signal **(D)**, weighted subtraction (Equation 1.5.7) is used for positive spike removal, giving  $y_{ds+}(t)$  **(E,F)**. The procedure is repeated for negative de-spiking with an input of  $-y_{ds+}(t)$  **(G,H)**.

**(2) Global filtering:** In sub-timeseries of six epochs,  $y_{ds}(t)$  is segmented into  $T_{on}$  and  $T_{off}$  intervals **(I)**. Minimization of the mean squared error  $\Delta(N_h)$  between the Fourier spectra  $Y_{ds,off}(f)$  **(J)** and  $\tilde{Y}_{on}(f, N_h)$  **(K,L)** is performed using Equations 1.5.8 to determine  $(h^{sf}, N_h^{sf})$  **(M)**.  $h^{sf}$  is used in Equation 1.5.5 with  $y_{ds}(t)$  as the input signal to yield the artifact-free EEG signal  $y_{sf}(t)$  **(N,O)**.

## 1.6 Thesis overview

The human brain is immensely complex and difficult to study. fMRI and EEG are the two most powerful modalities for studying the brain. fMRI images the brain over time with high spatial resolution yet poor temporal resolution, and in doing so indirectly measures neural activity in each voxel. Complementarily, EEG, using an array of scalp electrodes, directly measures neural activity with high temporal resolution yet poor spatial resolution. The complementary strengths of these two modalities have motivated much research using their combined, simultaneous acquisition. Despite the benefits of EEG-fMRI, there are a number of unique artifacts, the most detrimental one coming from the time-varying gradient field of fMRI interacting with and disrupting the EEG signal. For years, this gradient artifact has been the target of novel signal processing and prospective techniques for mitigation or prevention. However, removal of the gradient artifact and preservation of the signal throughout all EEG frequency bands remains an unresolved challenge.

This thesis introduces Schrödinger filtering, a new gradient artifact removal technique. Schrödinger filtering is based on semi-classical signal analysis (SCSA). In SCSA, an input signal is treated as an attractive potential in the Schrödinger operator.

The discrete spectrum of this operator contains a set of weighted squared eigenfunctions called Schrödinger components. Schrödinger components are pulse-shaped signals that individually describe one or more peaks of the input signal and have distinct energies ranging from high to low. SCSA reconstructs the input signal using the Schrödinger components and is therefore analogous to the discrete Fourier transform, which represents an input signal as a series of sinusoids of different frequencies. SCSA is particularly suited to gradient artifact removal since there are Schrödinger components that separately capture signal and artifact. Schrödinger filtering adapts SCSA for gradient artifact removal in two steps. Firstly, following AAS, the EEG signal is rid of gradient-related spikes by selectively removing high-energy Schrödinger components that represent the spikes. Secondly, following de-spiking, the signal is globally filtered by removing Schrödinger components corresponding to residual artifact. De-spiking improves the performance of global filtering as it facilitates a finer separation between artifact and signal. Schrödinger filtering also has the inherent benefit of denoising the signal.

On a publicly available dataset, Schrödinger filtering was implemented in a pipeline that first features average artifact subtraction (AAS)—a simple and effective staple in gradient artifact removal pipelines that yet results in residual gradient artifact. The Schrödinger filtering pipeline was compared against two popular pipelines: one that features AAS, temporal PCA, and ANC; and one that features AAS and manual spatial ICA. These latter two pipelines also apply bandpass filtering while the Schrödinger filtering pipeline does not. The Schrödinger filtering pipeline outperformed the other two pipelines across all EEG frequency bands based on a quantitative metric of EEG signal

preservation and performed comparably in terms of artifact removal. Schrödinger filtering, when combined with AAS, is therefore a robust solution for removal of the gradient artifact from EEG data.

In Chapter 2: Methods, details are given on the dataset, the Schrödinger filtering algorithm, the pipelines used, and the metrics of signal preservation and artifact removal. In Chapter 3: Results and Discussion, the performance of Schrödinger filtering is presented and discussed. In particular, the individual steps of de-spiking and global filtering, as well as their combination, are analyzed and compared against the two other pipelines, including according to the metrics of evaluation. In Chapter 4: Conclusions, the work of the thesis is recapitulated, including motivation, background, methods, results, and a brief discussion. Limitations and future directions of SCSA, Schrödinger filtering, and the present study are also given.

# 2 Methods

## 2.1 Dataset

A freely available dataset from the FMRI Artifact Slice Template Removal (FASTR)<sup>23</sup> toolbox website was analyzed ([fsl.fmrib.ox.ac.uk/eeglab/fmribplugin](http://fsl.fmrib.ox.ac.uk/eeglab/fmribplugin)). This dataset contains 30 channels of human scalp EEG arranged according to the 10-20 international system plus 1 channel of electrocardiography and 1 channel of electromyography. Only the 30 channels of EEG were analyzed. During scanning, the subject opened and closed their eyes in consecutive alternating 10-second intervals. All channels were sampled at 2048 Hz. The fMRI volume repetition time was 3 seconds and there were 21 slices per volume. There was a total of 40 volumes acquired, corresponding to 840 slices and 2 minutes of scanning. Data was also recorded for roughly 29 seconds before and 13 seconds after scanning. This data did not feature EEG-fMRI phase synchronization.

## 2.2 Schrödinger filtering algorithm

The Schrödinger filtering algorithm was organized into two main steps: (1) de-spiking and (2) global filtering (**Figure 1.12**). In the de-spiking step, low-order, high energy Schrödinger components, which nearly entirely depict data spikes, were linearly regressed from  $y_{aas}(t)$  to remove the spikes. In the global filtering step, the de-spiked signal  $\tilde{y}_{ds}(t)$  was reconstructed with  $(h^{sf}, N_h^{sf})$ , which were determined by minimizing the mean squared error between the magnitude spectra of the signal while the gradients were on and off, to provide the gradient artifact-free EEG signal  $y_{sf}(t)$ .

### 2.2.1 Step 1: de-spiking

Using the slice acquisition triggers, the slice acquisition epochs were segmented. The post-AAS signal  $y_{aas}(t)$  was fully reconstructed by SCSA (Equation 1.5.5) to provide  $\tilde{y}_{aas}(t)$  and the pair  $(h^*, N_h^*)$  for each epoch and each channel (**Figure 1.12A**). Positive de-spiking was performed as follows in three steps. (1) A positive peak was defined as a spike only if: (a) following polynomial detrending, the peak surpassed an empirically determined magnitude threshold of 3.5 times the mean absolute deviation (MAD) (**Figure 1.12B**); and (b) there existed a primary component  $y_I(t)$  for the spike (**Figure 1.12C**). Note that the de-trended signal was only used for spike definition. (2) Following 100-fold spline interpolation of  $\tilde{y}_{aas}(t)$ , the boundaries of a spike were determined as the two points straddling the spike that intersected with the trend (**Figure 1.12D**). (3) Weighted subtraction of primary and secondary components  $y_I(t)$  and  $y_{II}(t)$  (also interpolated) from  $\tilde{y}_{aas}(t)$  was performed (**Figure 1.12E**). Once all positive spikes within the epoch were removed, the signal was subsequently de-interpolated to yield

$y_{ds+}(t)$  (**Figure 1.12F**). The above de-spiking procedure was repeated on the vertical reflection of  $y_{ds+}(t)$  (**Figure 1.12G**) to remove the negative spikes. After negative de-spiking, the output signal was reflected back to yield  $y_{ds}(t)$  (**Figure 1.12H**).

### 2.2.2 Step 2: global filtering

Each channel's timeseries was divided into sub-timeseries of six epochs, resulting in 140 sub-timeseries. Per channel, the optimal  $(h^{sf}, N_h^{sf})$  were determined for only the first sub-timeseries and applied to all sub-timeseries (**Figure 1.12I**). This was computationally efficient and effective because  $(h^{sf}, N_h^{sf})$  was stable over the remaining sub-timeseries for each channel.

The first sub-timeseries was fully reconstructed by SCSA, yielding  $(h^*, N_h^*)$ .  $T_{on}$  and  $T_{off}$  (**Figure 1.12I**) were determined by magnitude-thresholding the raw timeseries (**Figure 1.8**) at 2.5% of the maximum. The magnitude spectrum  $Y_{ds,off}(f)$  of  $y_{ds}(t)$  during  $T_{off}$  was computed for the first sub-timeseries. Likewise, the magnitude spectrum  $\tilde{Y}_{ds,on}(f, N_h)$  of  $\tilde{y}_{ds}(t)$  during  $T_{on}$  for the first sub-timeseries was computed as a function of  $N_h$  up to  $N_h = N_h^*$  (**Figure 1.12JKL**). The pair of  $(h^{sf}, N_h^{sf})$  was then determined using Equations 1.5.8 (**Figure 1.12M**). All sub-timeseries  $\tilde{y}_{ds}(t)$  were finally filtered by SCSA with  $h = h^{sf}$  using Equation 1.5.5 to yield the artifact-free EEG signal  $y_{sf}(t)$  (**Figure 1.12NO**). For some channels, the minimum of the error function  $\Delta(N_h)$  of Equation 1.5.8a was broad, giving a range of suitable  $N_h^{sf}$  values. For these channels,  $N_h^{sf}$  was set to the empirically determined conservative value of 90 and the corresponding  $h^{sf}$  was determined.

## 2.3 Processing pipelines

Three pipelines were applied to the dataset in parallel: (1) a variant<sup>87</sup> of the FASTR<sup>23</sup> pipeline, which applies AAS, temporal PCA, LPF, and ANC; (2) a pipeline featuring AAS, LPF, and manual spatial ICA; and (3) the proposed Schrödinger filtering pipeline that features only AAS and Schrödinger filtering. Except for ICA and Schrödinger filtering, all processing steps were performed using Flexible Artifact Correction and Evaluation Toolbox (FACET)<sup>87</sup>—an open-source Matlab (MathWorks, Natick, MA) toolbox dedicated to gradient artifact removal. FACET handles the data in EEGLAB<sup>88</sup> structure array format and applies its pipeline per-channel. ICA was performed using FastICA on Matlab (research.ics.aalto.fi/ica/fastica)<sup>79</sup>. Schrödinger filtering was performed using Matlab scripts available at [github.com/gbenigno/schrodinger\\_filtering](https://github.com/gbenigno/schrodinger_filtering). The three pipelines were divided into common pre-processing steps up to and including AAS, followed by pipeline-specific steps. A schematic of the pipelines is shown in **Figure 2.1**.

There were four common pre-processing steps. First, a high-pass Gaussian filter was applied in the frequency domain at 1 Hz to remove baseline drifts. Second, slice timing alignment was performed to correct for the non-synchronicity between the clocks of the EEG and the gradients. Third, the volume artifact—the short stretch of data between the last slice epoch of one volume and the first slice epoch of the next volume—was corrected<sup>29</sup>. Fourth, AAS was performed using a variant of Allen *et al.*'s original method<sup>22</sup> that is based on<sup>29</sup>.

For the Schrödinger filtering pipeline, the post-AAS signal  $y_{aas}(t)$  was processed by Schrödinger filtering to yield an artifact-free EEG signal  $y_{sf}(t)$  using the de-spiking

and global filtering procedures as described in Sections 1.5.2 and 2.2.

For the ICA pipeline,  $y_{aas}(t)$  was low-pass-filtered at 150 Hz before performing ICA across the 30 EEG channels. Each of the 30 independent components generated was inspected in the time and frequency domains. Components whose variance appeared to significantly characterize residual gradient artifact were removed, yielding  $y_{ica}(t)$ . ICA's ability to separate signal from artifact was limited by the low number of independent components, which was limited by the number of input signals—*i.e.*, 30. As such, 25 of the 30 components were found to contain significant artifact.

For the FASTR variant pipeline, temporal PCA was used to form an optimal basis set (OBS) that described the majority of the variance of the post-AAS residual artifact of  $y_{aas}(t)$ . The OBS was added to the AAS artifact template and AAS was repeated with the updated template before 150-Hz high-pass-filtering and ANC, yielding  $y_{fastr}(t)$ .

## Gradient artifact removal pipelines

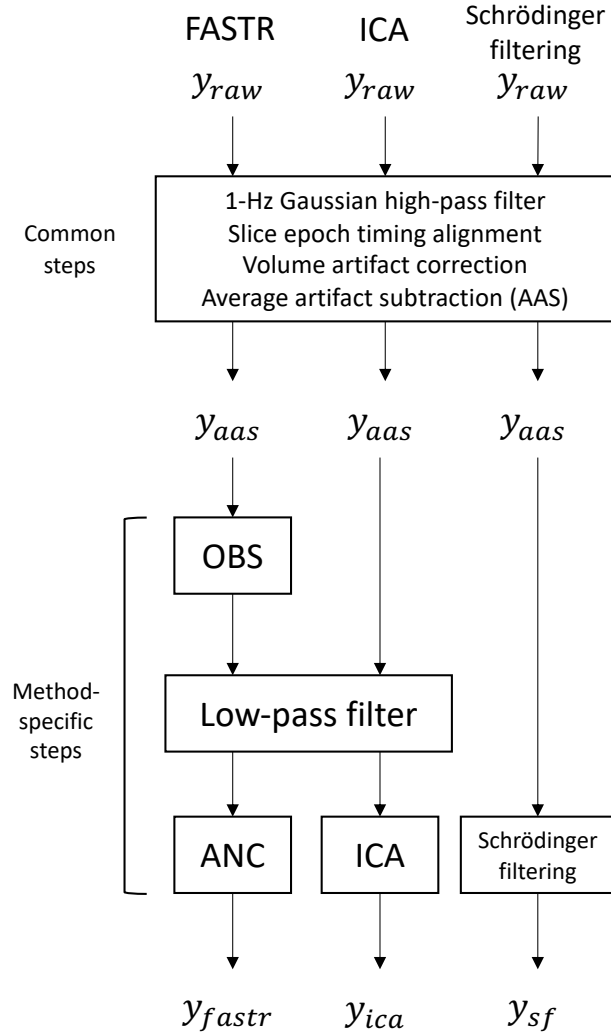


**Figure 2.1:** Flowchart of the three gradient artifact removal pipelines.

(1) a variant of FASTR; (2) a pipeline that incorporates manual spatial ICA; and (3) the proposed Schrödinger filtering pipeline. The three pipelines share the common steps of a 1-Hz frequency-domain Gaussian high-pass filter, slice epoch timing alignment, volume artifact correction, and AAS. The signal  $y_{aas}(t)$  following the common steps is then subject to pipeline-specific steps. For the FASTR variant pipeline, temporal PCA is performed and the first few principal components, which form an OBS, are added to the artifact template generated by AAS to form an updated template. AAS is repeated with the updated template. Following the OBS step, the signal is low-pass-filtered at 150 Hz and then subjected to ANC to give  $y_{FASTR}(t)$ . For the ICA pipeline, low-pass filtering at 150 Hz is applied on  $y_{aas}(t)$ . Then, manual spatial ICA is used to remove independent components classified as mostly containing gradient artifact. The output is  $y_{ica}(t)$ . For the Schrödinger filtering pipeline,  $y_{aas}(t)$  is processed by Schrödinger filtering, which entails de-spiking of gradient-related spikes and global filtering in which Schrödinger components belonging to gradient artifact throughout the signal are removed from the de-spiked signal. The output is  $y_{sf}(t)$ .

## 2.4 Evaluation of performance

The performances of the three techniques were quantitatively compared by measuring the amount of EEG preserved and the amount of gradient artifact removed. This was achieved using two metrics: median residual activity (MRA) and median fraction at slice frequencies (MFSF), respectively.

### 2.4.1 Median residual activity (MRA)

MRA is a measure of the quantity of preserved EEG signal following gradient artifact removal. MRA was first introduced by Allen *et al.*<sup>22</sup>. The authors binned and averaged the Fourier magnitudes with and without scanning (although still in the scanner) into delta, theta, alpha, and beta bands (0.8-4, 4-8, 8-12, and 12-24 Hz, respectively). They then proceeded to calculate the percent differences per band and per channel. The signal acquired without scanning was used as a gradient artifact-free reference. For each band, the median value over all channels was deemed the MRA.

Since the signals acquired with and without scanning are considerably separated in time, their EEG activity is likely different. We therefore used an alternative definition of MRA in which only the signal during  $T_{off}$ , which is assumed free of gradient artifact, is analyzed. The percent difference was taken of the signal processed by the Schrödinger filtering pipeline, the FASTR variant, and the ICA pipeline during  $T_{off}$  relative to the post-AAS signal during  $T_{off}$ . This definition of MRA is likely more accurate at estimating EEG preservation. The per-band MRA for each of the three methods is

$$MRA_{method}^{band} = \text{median} \left( \frac{\bar{Y}_{method,off}^{band} - \bar{Y}_{aas,off}^{band}}{\bar{Y}_{aas,off}^{band}} \right), \quad (2.1)$$

where  $\bar{Y}_{aas,off}^{band}$  and  $\bar{Y}_{method,off}^{band}$  are the per-band magnitude spectral densities of  $y_{method}$  and  $y_{aas}$ , respectively, during  $T_{off}$ ;  $y_{method}$  refers to one of  $y_{fastr}$ ,  $y_{ica}$ , or  $y_{sf}$ ; and the median is taken across the thirty channels. We analyzed traditional EEG bands as high as upper-gamma (1-4, 4-8, 8-12, 12-30, and 30-120 Hz).

## 2.4.2 Median fraction at slice frequencies (MFSF)

MFSF is a measure of gradient artifact removal. Niazy *et al.*<sup>23</sup> performed a measurement similar to MFSF in which the ratio of the power spectral densities were taken at the fundamental (7 Hz) and the first four harmonic frequencies (14, 21, 28, and 35 Hz) ( $\pm 1$  Hz) of the slice-wise gradient artifact before and after a particular processing step. The spectral powers we used corresponded to the timeseries during  $T_{on}$ , where the gradient artifact is. By omitting data during  $T_{off}$ , which is mostly EEG signal, the specificity is increased of measuring artifact reduction and not signal loss. The MFSF for a single slice frequency  $f$  of each method is

$$MFSF_{method}^{(f)} = \text{median} \left( \frac{\hat{Y}_{method,on}^{(f)}}{\hat{Y}_{aas,on}^{(f)}} \right), \quad (2.2)$$

where  $\hat{Y}_{aas,on}^{(f)}$  and  $\hat{Y}_{method,on}^{(f)}$  are the power spectral densities (at slice frequency  $f \pm 1$  Hz) of  $y_{method}$  and  $y_{aas}$ , respectively, during  $T_{on}$ , and the median is taken across the thirty channels. We analyzed up to the 119-Hz harmonic.

# 3 Results and Discussion

## 3.1 De-spiking

In some channels, the EEG amplitude was comparable to or greater than that of the post-AAS artifact. In such channels, spikes, defined as peaks of the de-trended signal that surpassed the threshold of 3.5 times the MAD, were usually not present. In other channels where spikes were prevalent, there existed epochs (commonly around the middle of acquisition) in which there were no spikes. It is worth emphasizing that where spikes were not identified, de-spiking was not performed, thereby appropriately preserving signal.

To illustrate the benefit of de-spiking, **Figure 3.1** displays  $y_{ds}(t)$  compared to  $y_{aas}(t)$  for six epochs of the F8 channel, which is among the channels with the highest-amplitude post-AAS gradient artifact relative to the respective EEG signal, and especially the highest-amplitude gradient-related spikes. In the frequency domain, the benefit of de-spiking is apparent, as the magnitudes at the artifact slice frequencies are reduced while

the activity elsewhere in the spectrum is unaffected.

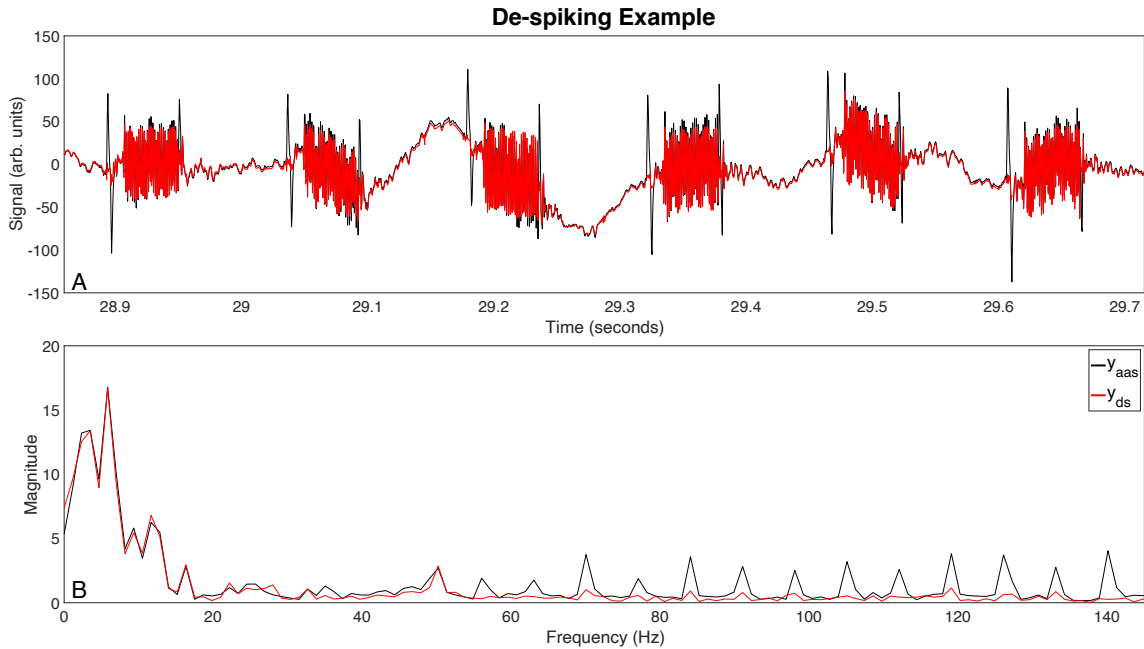


**Figure 3.1:** Effect of de-spiking.

Effect of de-spiking in reducing the contamination of large spikes in  $y_{aas}(t)$  prior to global filtering. **(A)** The timeseries of six epochs before (black) and after (red) despiking. **(B)** The magnitude of the corresponding spectra. The slice acquisition frequencies of 7, 14, 21, ... Hz are frequencies at which there is significant artifact. At such frequencies 56 Hz and above, it is evident that the artifact is reduced.

The benefit of de-spiking on the performance of Schrödinger filtering in reducing the gradient artifact is also evident. **Figure 3.2AB** shows six epochs of the F8 channel for two cases of filtering: AAS→global filtering and AAS→de-spiking→global filtering. From the timeseries in panel A, it is clear that the gradient-related spikes are reduced in the latter case. This is accompanied by a set of magnitude spectra in panel B at the upper slice acquisition frequencies (*i.e.*, 56, 63, ... Hz) that are reduced as well. **Figure 3.2C** shows the improvement over all channels. A box-and-whisker plot of the MFSF—a measure of gradient artifact removal—for all channels is displayed at the fundamental

slice acquisition frequency of 7 Hz and harmonics up to and including 119 Hz. The MFSF is consistently lower at each of the frequencies.

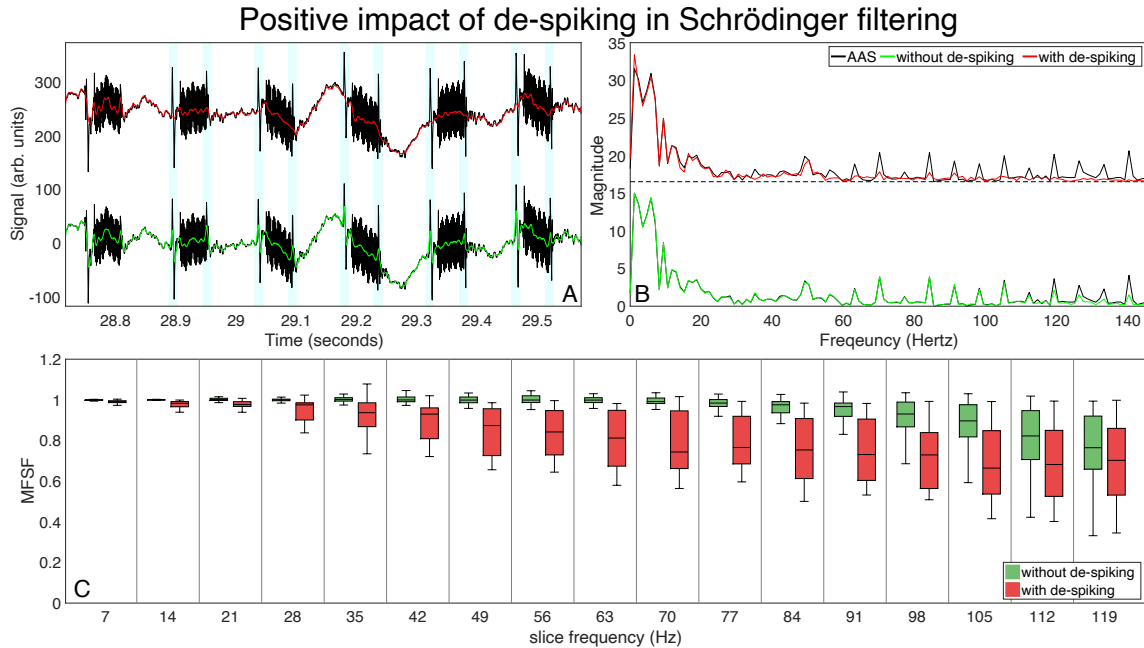


**Figure 3.2:** Positive impact of de-spiking in Schrödinger filtering.

The F8 channel, which has a large residual gradient artifact relative to its EEG signal, is shown. (A) The timeseries of the six epochs is de-spiked when using the corresponding step as indicated by the light-blue stripes. (B) The positive impact of despiking is evident in the spectra at the slice acquisition frequencies of 7, 14, ... Hz—especially those at and above 56 Hz. (C) A box-and-whisker plot of the MFSF, which measures gradient artifact removal, showing that Schrödinger filtering, when including despiking, results in better removal of the gradient artifact.

## 3.2 Global filtering

To illustrate the overall result of the Schrödinger filtering pipeline, which uses AAS followed by Schrödinger filtering, **Figure 3.3** and **Figure 3.4** each show the timeseries and corresponding FFTs of six slice epochs for channels F8 and T4, respectively, as produced by all three pipelines. These two channels are examples of channels that have artifact amplitudes greater than or comparable to the EEG signal, respectively. In **Figure**

3.3, it is apparent that for the Schrödinger filtering pipeline, de-spiking minimized gradient-related spikes compared to the other techniques. In **Figure 3.4**, the ability of global filtering in retaining EEG signal is displayed.

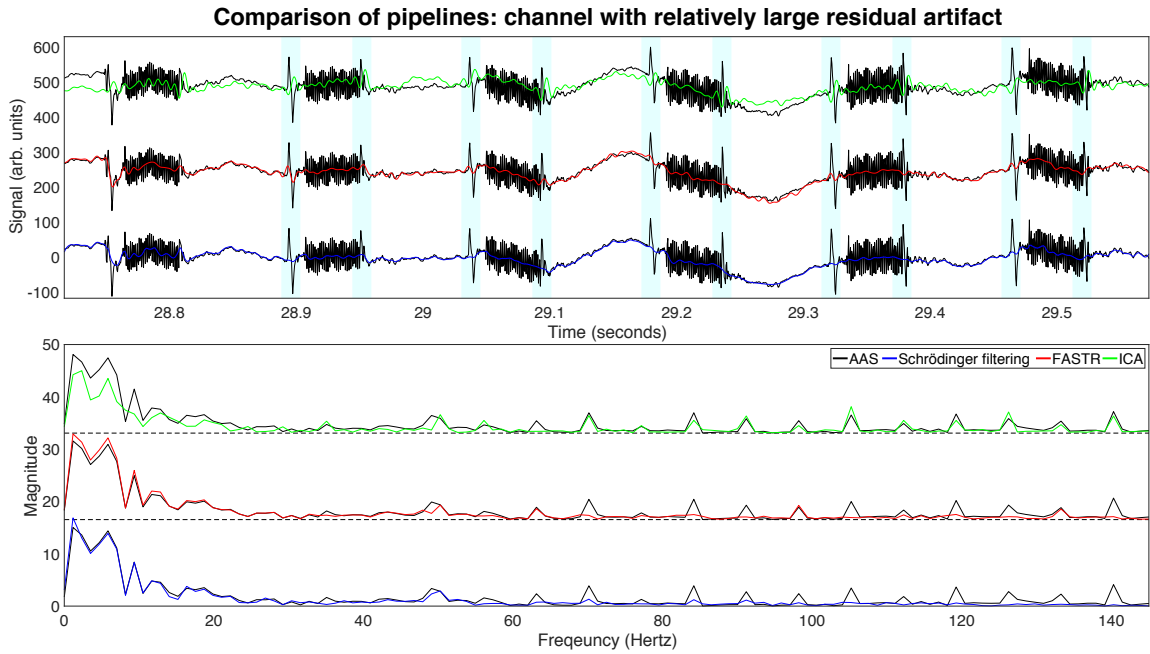


**Figure 3.3:** Performances of the pipelines for channel with large residual artifact. The performances of the three pipelines for the F8 channel, which has a large residual gradient artifact relative to its EEG signal. EEG signal is well-preserved using Schrödinger filtering, with significant reduction of spikes as outlined by the light-blue stripes.

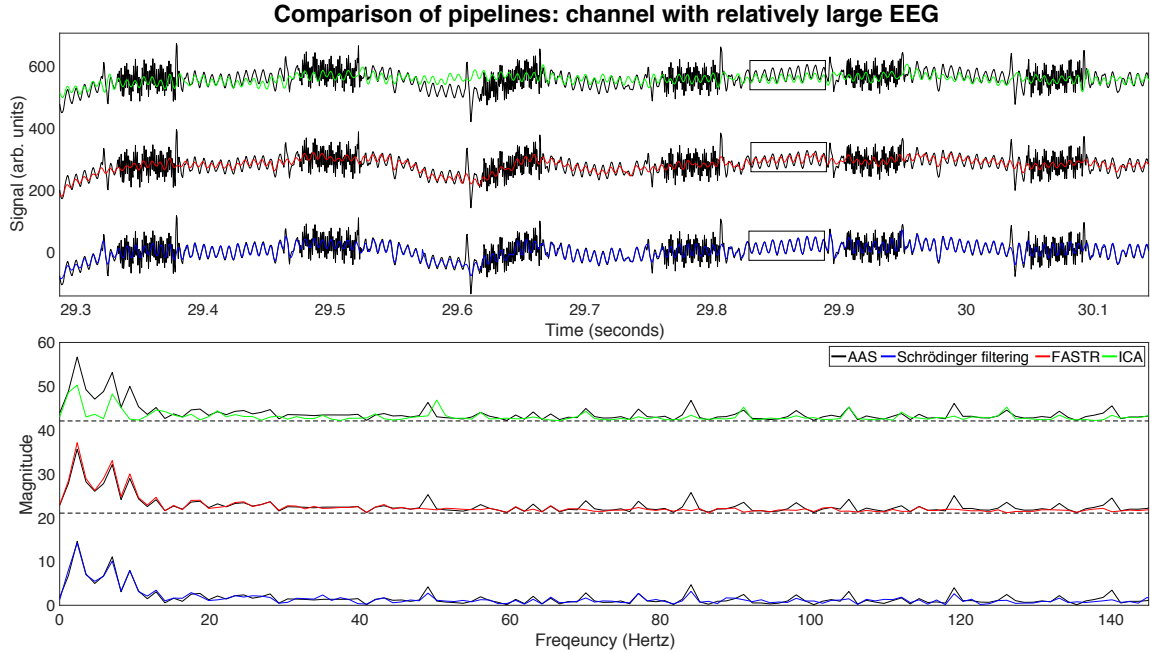


**Figure 3.4:** Performances of the pipelines for channel with small residual artifact. The performances of the three pipelines for the T4 channel, which has residual gradient artifact comparable to its EEG signal in magnitude. Schrödinger filtering best preserves EEG signal, as outlined by the rectangles. For Schrödinger filtering, the signal is unaffected in the artifact-free  $T_{off}$  region, while this is not the case for the other pipelines.

Across all channels and all 840 epochs, the Schrödinger filtering pipeline outperformed the other two pipelines in preserving EEG signal as measured by MRA (**Figure 3.5**). For all EEG frequency bands, the Schrödinger filtering pipeline has near-zero MRA-values with a smaller overall interquartile range.

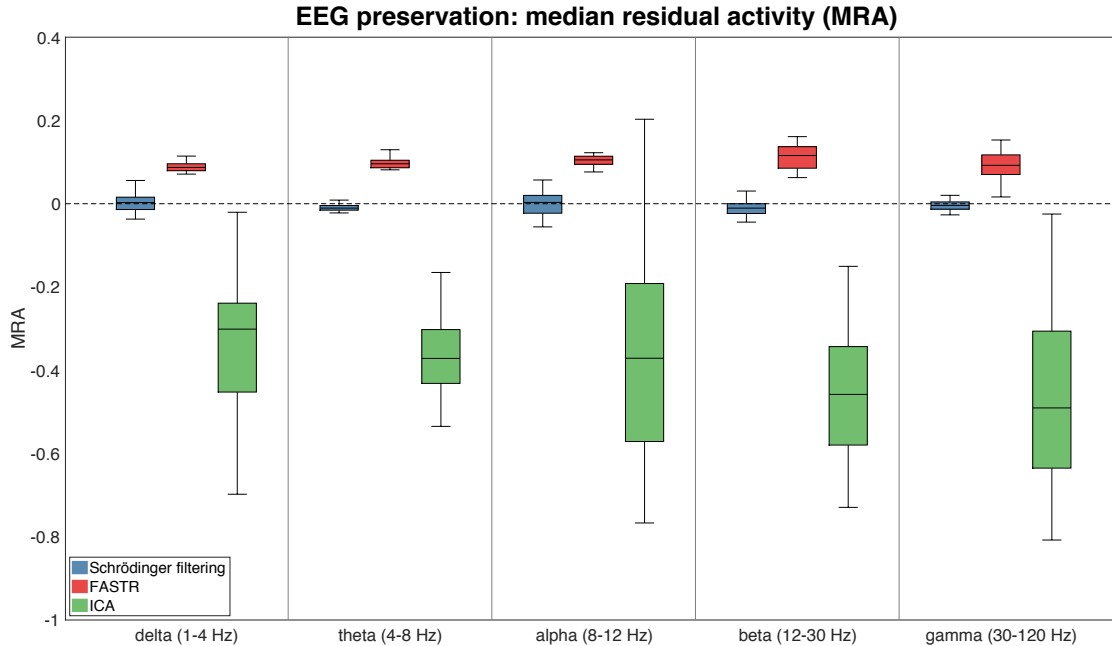


**Figure 3.5:** MRA comparison of the three pipelines.

Band-wise box-and-whisker plot of median residual activity as a metric of EEG preservation across all 30 channels and all epochs. Schrödinger filtering preserves EEG better than the FASTR variant or the ICA pipeline, as indicated by MRA-values closer to zero and a smaller overall interquartile range.

To compare artifact removal across the pipelines, **Figure 3.6** shows a box-and-whisker plot of MFSF for the fundamental slice frequency of 7 Hz and harmonics up to 119 Hz. At low frequencies, the ICA pipeline performs better than the Schrödinger filtering pipeline and the FASTR variant for some channels. However, the ICA pipeline's good MFSF values are accompanied by poor signal preservation, which is evident in its poor MRA results, as well as highly variant performance across the channels. Overall, the FASTR variant and the Schrödinger filtering pipeline perform comparably in consistently removing an appreciable amount of artifact.

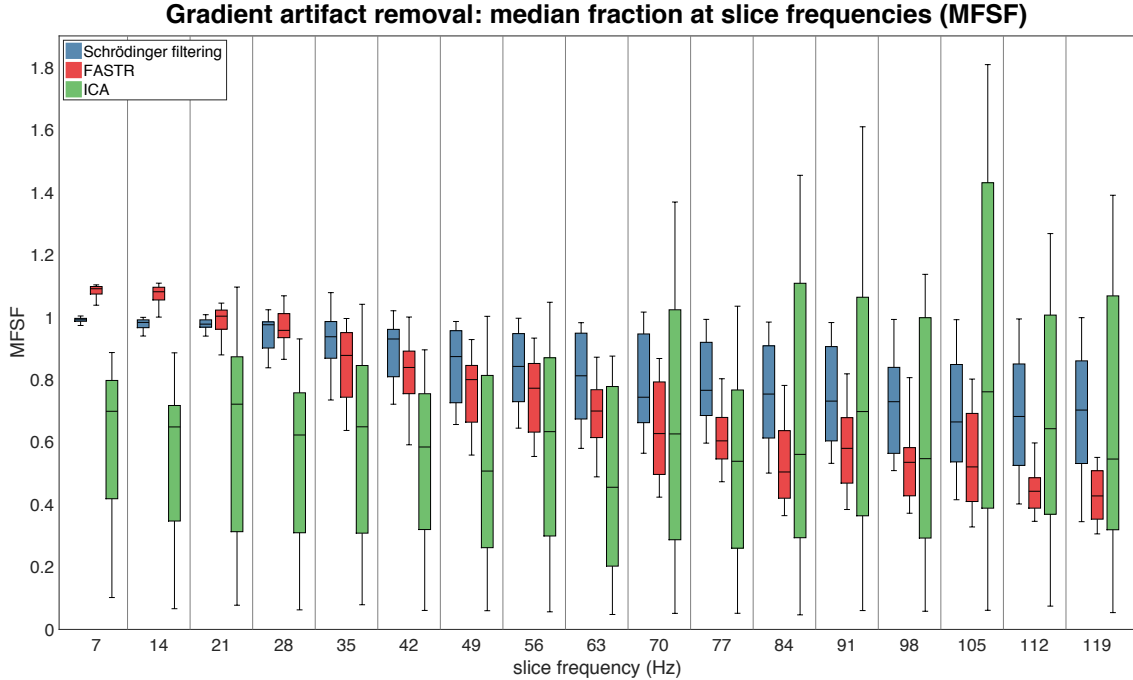


**Figure 3.6:** MFSF comparison of the three pipelines.

Assessment of gradient artifact removal by measurement of median fraction at slice frequencies (MFSF) for the three pipelines across all channels and all epochs. At low frequencies, the ICA pipeline performs best, although this is accompanied with signal loss as indicated by poor MRA results. Overall, the three pipelines perform comparably in removing a significant amount of artifact.

The global filtering step of Schrödinger filtering separates Schrödinger components representing the EEG signal and those describing the rest of the signal, which not only contain residual gradient artifact but also any additive noise incurred during data recording. Global filtering is therefore a denoising technique as well as an artifact removal technique.

Schrödinger filtering preserved the increases in alpha activity in posterior brain regions that followed subject eye-closing. **Figure 3.7** shows Schrödinger-filtered signals from seven posteriorly placed electrodes. It is apparent from the traces that alpha activity increases are present in ten-second intervals. This is in accord with the task paradigm of alternating ten-second periods of eye closing and opening.

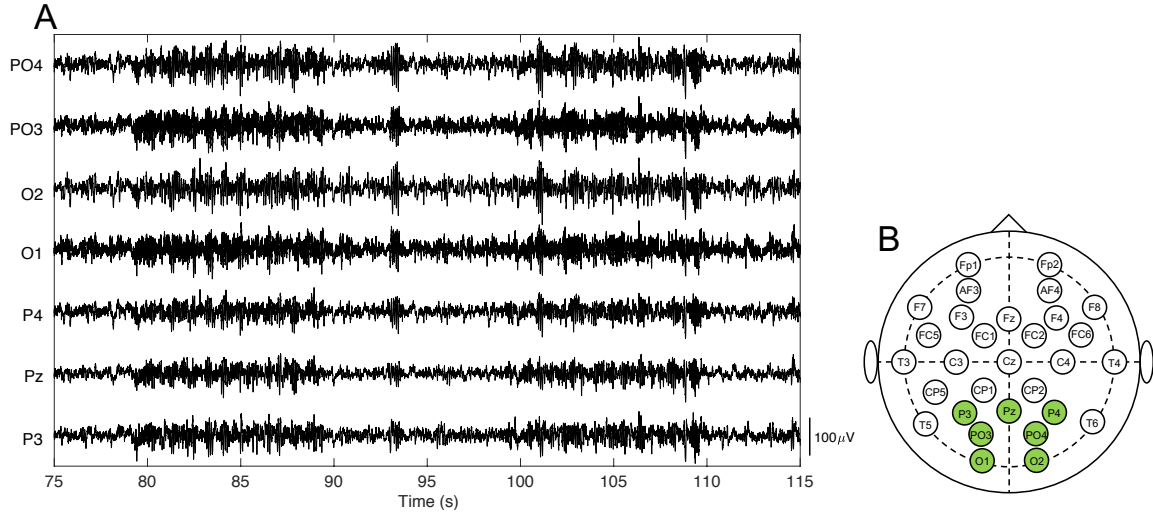


**Figure 3.7:** Preservation of increased alpha-band activity following eye-closing. In posterior brain regions, alpha activity diminishes shortly after eye-opening and increases shortly after eye-closing. In the present dataset, the subject opened and closed their eyes in alternating ten-second intervals. Shown in (A) are the signals of seven posteriorly placed electrodes (B) following the Schrödinger filtering pipeline. These traces preserve alpha bursts and alpha blocking, which are localized to alternating ten-second intervals in accord with the task paradigm.

Signal preservation and artifact removal are critical to an EEG-fMRI analysis pipeline. The Schrödinger filtering pipeline overall outperformed the other two pipelines with respect to preserving the essential features of the EEG. Moreover, the Schrödinger filtering pipeline was consistent across frequency bands, including upper-gamma, in preserving signal, whereas the ICA pipeline performed poorly overall and with large variance across all bands, and the FASTR variant’s performance diminished for higher bands. The Schrödinger filtering pipeline is therefore preferred since it facilitates analysis of high-frequency—*i.e.*, gamma-band—EEG in scalp EEG-fMRI experiments, which is most sensitive to artifact and is usually avoided.

# 4 Conclusions

## 4.1 Summary

EEG data acquired during fMRI, despite decades of work, faces the unresolved issue of removing the large-amplitude artifacts that arise from the time-varying gradient fields present during scanning. We presented a gradient artifact removal pipeline in which the new Schrödinger filtering technique is performed following average artifact subtraction (AAS). Schrödinger filtering is derived from semi-classical signal analysis (SCSA), which uses the Schrödinger operator to decompose an input signal into Schrödinger components of distinct energies. Schrödinger filtering comprises two steps, beginning with de-spiking, in which high-energy Schrödinger components corresponding to gradient-related spikes in the post-AAS signal are removed. This is followed by global filtering in which the EEG signal is extracted from the de-spiked signal. Global filtering manipulates SCSA so as to omit residual post-AAS artifact.

Compared to two other pipelines—a variant of FASTR and a pipeline

incorporating manual spatial ICA—the Schrödinger filtering pipeline best preserved the EEG signal characteristics across all frequency bands, up to and including upper-gamma, with significant reduction of the gradient artifact. Since Schrödinger filtering manipulates energy-based Schrödinger components for signal decomposition and reconstruction, our pipeline does not require frequency-domain bandpass filtering, unlike other pipelines. Also unique to Schrödinger filtering, the global filtering step simultaneously denoises the signal and removes artifact. The Schrödinger filtering pipeline is fully automatic for data that features pauses between each slice acquisition—the cost function used in the global filtering step relies on these periods. For data without such pauses, the pipeline is semi-automatic. Overall, Schrödinger filtering facilitates accurate EEG signal extraction and is therefore a robust method for gradient artifact removal of EEG data acquired during fMRI.

## 4.2 Limitations and future directions

SCSA is a young signal analysis technique. (The earliest record of publication is from 2009<sup>89,90</sup>.) Thus, research is ongoing in elucidating its mathematical intricacies. For instance, the Schrödinger series  $\tilde{s}_h(t) = 4h \sum_{n=1}^{N_h} \kappa_{h,n} \psi_{h,n}^2(t)$  (Equation 1.5.5) does not contain an orthonormal basis, making global filtering (Section 1.5.2.2) a nonlinear operation. This is unlike filtering using the Fourier or wavelet transforms. Nonlinear filters are useful for highly nonlinear systems, such as the system studied in this thesis: the overlapping frequency spaces of the EEG signal and gradient artifact. One shortcoming of nonlinear filters is that they are difficult to interpret, making it difficult to fine-tune the filtering parameters<sup>91</sup>. Therefore, to improve the efficiency and

effectiveness of filtering applications of SCSA, further mathematical exploration is required—*e.g.*, whether closed-form expressions of the Schrödinger components and of  $\tilde{s}_h(t)$  can be predicted from a given pair of  $s(t)$  and  $h$ ; and whether the Schrödinger series can be explicitly related to the Fourier transform by means of a describing function<sup>92</sup> or similar framework. The latter would be valuable for cases where the frequency distribution of a time-domain signal is of interest, such as in this thesis.

The dataset analyzed in this work was recorded with an MRI pulse sequence that pauses between slice acquisitions for roughly as long as the acquisitions themselves. This pulse sequence resulted in relatively long  $T_{off}$ .  $T_{off}$  is an integral variable of the cost function (Equation 1.5.8a) used for automating the global filtering step of the algorithm. Contemporary pulse sequences in EEG-fMRI do not typically pause for as long between slice acquisitions. However, the de-spiking step is fully automatic regardless of the length of  $T_{off}$ , and global filtering does not fundamentally rely on  $T_{off}$ . The present work demonstrates the ability of Schrödinger filtering in separating EEG signal from residual gradient artifact following AAS. Therefore, on any data, including data acquired with short  $T_{off}$ , Schrödinger filtering can be applied semi-automatically—*i.e.*, by manually selecting  $N_h^{sf}$  during global filtering. Future efforts directed at machine learning and the mathematical research described in the previous paragraph are expected to help fully automate Schrödinger filtering in data with short  $T_{off}$ .

All code used in this thesis is available online on GitHub ([github.com/gbenigno/shcrodingier\\_filtering](https://github.com/gbenigno/shcrodingier_filtering)) with instructions for implementation on one's own computer. The GitHub platform accommodates miscellaneous improvements suggested by users. The code is written in Matlab and is not optimized for speed. An

opportune future step for this work is speeding up the execution of the code. Code may be sped up in a number of ways, including conversion to a lower-level language (*e.g.*, C++) and parallelization. Schrödinger filtering may be extended to the analysis of other types of signals such as invasive electrophysiological local field potentials and fMRI timeseries.

Finally, shortcomings of the data must be addressed. There was only two minutes of recorded data for each channel, but since there was a large number (thirty) of recorded channels and since the sampling rate was high (2048 Hz), the dataset used was sufficient for this proof of concept. However, since the data is from only one subject and from a single recording apparatus, the algorithm may have overfitted based on unique characteristics of the subject (*e.g.*, below-average alpha activity) and the apparatus (*e.g.*, above-average post-AAS gradient artifact amplitude). To ensure that the performance of Schrödinger filtering in this thesis is representative of subjects and EEG-fMRI recording apparatuses in general, inclusion of multiple subjects across multiple sites is necessary.

## References

1. Herculano-Houzel, S. The human brain in numbers: a linearly scaled-up primate brain. *Front. Hum. Neurosci.* **3**, 31 (2009).
2. Wong, T. M. *et al.* *IBM Research Report: 10<sup>14</sup>*. (2012).
3. Lopes da Silva, F. Chapter 2: EEG: Origin and Measurement. in *EEG-fMRI: Physiological Basis, Technique, and Applications* (eds. Mulert, C. & Lemieux, L.) 19–38 (Springer, 2010).
4. Horovitz, S. G. *et al.* Low frequency BOLD fluctuations during resting wakefulness and light sleep: A simultaneous EEG-fMRI study. *Hum. Brain Mapp.* **29**, 671–682 (2008).
5. Laufs, H. Endogenous brain oscillations and related networks detected by surface EEG-combined fMRI. *Hum. Brain Mapp.* **29**, 762–769 (2008).
6. Nir, Y. *et al.* Interhemispheric correlations of slow spontaneous neuronal fluctuations revealed in human sensory cortex. *Nat. Neurosci.* **11**, 1100–1108 (2008).
7. Gotman, J., Kobayashi, E., Bagshaw, A. P., Bénar, C.-G. & Dubeau, F. Combining EEG and fMRI: A multimodal tool for epilepsy research. *J. Magn. Reson. Imaging* **23**, 906–920 (2006).
8. Bénar, C.-G. *et al.* Quality of EEG in simultaneous EEG-fMRI for epilepsy. *Clin. Neurophysiol.* **114**, 569–580 (2003).
9. Lemieux, L. *et al.* Event-Related fMRI with Simultaneous and Continuous EEG: Description of the Method and Initial Case Report. *Neuroimage* **14**, 780–787 (2001).
10. Villringer, A., Mulert, C. & Lemieux, L. Chapter 1: Principles of Multimodal Functional Imaging and Data Integration. in *EEG-fMRI: Physiological Basis, Technique, and Applications* (eds. Mulert, C. & Lemieux, L.) 3–17 (Springer, 2010).
11. Ianetti, G. D. & Mouraux, A. Chapter 18: Combining EEG and fMRI in Pain Research. in *EEG-fMRI: Physiological Basis, Technique, and Applications* (eds. Mulert, C. & Lemieux, L.) 365–384 (Springer, 2010).
12. Lopes da Silva, F. & Van Rotterdam, A. Chapter 5: Biophysical Aspects of EEG and Magnetoencephalogram Generation. in *Electroencephalography: Basic principles, clinical applications, and related fields* 107–126 (Wolters Kluwer, 2005).
13. Pauling, L. & Coryell, C. D. The Magnetic Properties and Structure of Hemoglobin, Oxyhemoglobin and Carbonmonoxyhemoglobin. *Proc. Natl. Acad. Sci.* **22**, 210–216 (1936).
14. Ogawa, S., Lee, T. -M, Nayak, A. S. & Glynn, P. Oxygenation-sensitive contrast in magnetic resonance image of rodent brain at high magnetic fields. *Magn. Reson. Med.* **14**, 68–78 (1990).
15. Ogawa, S. *et al.* Functional brain mapping by blood oxygenation level-dependent contrast magnetic resonance imaging. A comparison of signal characteristics with a biophysical model. *Biophys. J.* **64**, 803–812 (1993).
16. Ogawa, S., Lee, T. M., Kay, A. R. & Tank, D. W. Brain magnetic resonance

- imaging with contrast dependent on blood oxygenation. *Proc. Natl. Acad. Sci. U. S. A.* **87**, 9868–9872 (1990).
17. Heeger, D. J. & Ress, D. What does fMRI tell us about neuronal activity? *Nat. Rev. Neurosci.* **3**, 142–151 (2002).
  18. Matthews, P. M., Honey, G. D. & Bullmore, E. T. Applications of fMRI in translational medicine and clinical practice. *Nat. Rev. Neurosci.* **7**, 732–744 (2006).
  19. Huettel, S. A., Song, A. W. & McCarthy, G. Chapter 7: BOLD fMRI: Origins and Properties. in *Functional Magnetic Resonance Imaging* 193–242 (Sinauer Associates, Inc., 2008).
  20. Siniatchkin, M. & Dubeau, F. Chapter 17: EEG-fMRI in Children with Epilepsy. in *EEG-fMRI: Physiological Basis, Technique, and Applications* (eds. Mulert, C. & Lemieux, L.) 349–362 (Springer, 2010).
  21. Anami, K. *et al.* Stepping stone sampling for retrieving artifact-free electroencephalogram during functional magnetic resonance imaging. *Neuroimage* **19**, 281–295 (2003).
  22. Allen, P. J., Josephs, O. & Turner, R. A method for removing imaging artifact from continuous EEG recorded during functional MRI. *Neuroimage* **12**, 230–239 (2000).
  23. Niazy, R. K., Beckmann, C. F., Iannetti, G. D., Brady, J. M. & Smith, S. M. Removal of FMRI environment artifacts from EEG data using optimal basis sets. *Neuroimage* **28**, 720–737 (2005).
  24. Mandelkow, H., Halder, P., Boesiger, P. & Brandeis, D. Synchronization facilitates removal of MRI artefacts from concurrent EEG recordings and increases usable bandwidth. *Neuroimage* **32**, 1120–1126 (2006).
  25. Hoffmann, A. *et al.* Electroencephalography during functional echo-planar imaging: Detection of epileptic spikes using post-processing methods. *Magn. Reson. Med.* **44**, 791–798 (2000).
  26. Grouiller, F. *et al.* A comparative study of different artefact removal algorithms for EEG signals acquired during functional MRI. *Neuroimage* **38**, 124–137 (2007).
  27. Chowdhury, M. E. H., Mullinger, K. J., Glover, P. & Bowtell, R. Reference layer artefact subtraction (RLAS): A novel method of minimizing EEG artefacts during simultaneous fMRI. *Neuroimage* **84**, 307–319 (2014).
  28. Steyrl, D., Krausz, G., Koschutnig, K., Edlinger, G. & Müller-Putz, G. R. Reference layer adaptive filtering (RLAF) for EEG artifact reduction in simultaneous EEG-fMRI. *J. Neural Eng.* **14**, 026003 (2017).
  29. van der Meer, J. N., Tijssen, M. A. J., Bour, L. J., van Rootselaar, A. F. & Nederveen, A. J. Robust EMG-fMRI artifact reduction for motion (FARM). *Clin. Neurophysiol.* **121**, 766–776 (2010).
  30. Moosmann, M. *et al.* Realignment parameter-informed artefact correction for simultaneous EEG-fMRI recordings. *Neuroimage* **45**, 1144–1150 (2009).
  31. Ferreira, J. L., Wu, Y., Besseling, R. M. H., Lamerichs, R. & Aarts, R. M. Gradient Artefact Correction and Evaluation of the EEG Recorded Simultaneously with fMRI Data Using Optimised Moving-Average. *J. Med. Eng.* **2016**, 9614323 (2016).
  32. Negishi, M., Abildgaard, M., Nixon, T. & Todd Constable, R. Removal of time-

- varying gradient artifacts from EEG data acquired during continuous fMRI. *Clin. Neurophysiol.* **115**, 2181–2192 (2004).
33. Ryali, S., Glover, G. H., Chang, C. & Menon, V. Development, validation, and comparison of ICA-based gradient artifact reduction algorithms for simultaneous EEG-spiral in/out and echo-planar fMRI recordings. *Neuroimage* **48**, 348–361 (2009).
  34. Acharjee, P. P., Phlypo, R., Wu, L., Calhoun, V. D. & Adali, T. Independent Vector Analysis for Gradient Artifact Removal in Concurrent EEG-fMRI Data. *IEEE Trans. Biomed. Eng.* **62**, 1750–1758 (2015).
  35. Goldman, R. I., Stern, J. M., Engel, J. & Cohen, M. S. Acquiring simultaneous EEG and functional MRI. *Clin. Neurophysiol.* **111**, 1974–1980 (2000).
  36. Goldman, R. I., Stern, J. M., Engel, J., Cohen, M. S. & Cohen, M. S. Simultaneous EEG and fMRI of the alpha rhythm. *Neuroreport* **13**, 2487–92 (2002).
  37. Kruggel, F., Wiggins, C. J., Herrmann, C. S. & von Cramon, D. Y. Recording of the event-related potentials during functional MRI at 3.0 Tesla field strength. *Magn. Reson. Med.* **44**, 277–282 (2000).
  38. Ritter, P., Freyer, F., Curio, G. & Villringer, A. High-frequency (600 Hz) population spikes in human EEG delineate thalamic and cortical fMRI activation sites. *Neuroimage* **42**, 483–490 (2008).
  39. Pan, W. *et al.* Simultaneous fMRI and Electrophysiology in the Rodent Brain. *J. Vis. Exp.* e1901 (2010). doi:10.3791/1901
  40. Mantini, D. *et al.* Complete artifact removal for EEG recorded during continuous fMRI using independent component analysis. *Neuroimage* **34**, 598–607 (2007).
  41. Abreu, R., Leal, A. & Figueiredo, P. EEG-Informed fMRI: A Review of Data Analysis Methods. *Front. Hum. Neurosci.* **12**, 29 (2018).
  42. Laleg-Kirati, T.-M., Crépeau, E. & Sorine, M. Semi-classical signal analysis. *Math. Control. Signals, Syst.* **25**, 37–61 (2013).
  43. Huettel, S., Song, A. & McCarthy, G. Chapter 3: Basic Principles of Signal Generation. in *Functional Magnetic Resonance Imaging* 57–88 (Sinauer Associates, Inc., 2008).
  44. Huettel, S., Song, A. & McCarthy, G. Chapter 4: Basic Principles of MR Image Formation. in *Functional Magnetic Resonance Imaging* 89–120 (Sinauer Associates, Inc., 2008).
  45. Borogovac, A. & Asllani, I. Arterial Spin Labeling (ASL) fMRI: Advantages, Theoretical Constrains and Experimental Challenges in Neurosciences. *Int. J. Biomed. Imaging* **2012**, 1–13 (2012).
  46. Lu, H. & Zijl, P. van. A review of the development of Vascular-Space-Occupancy (VASO) fMRI. *Neuroimage* **62**, 736 (2012).
  47. Ogawa, S. *et al.* Intrinsic signal changes accompanying sensory stimulation: Functional brain mapping with magnetic resonance imaging. *Proc. Natl. Acad. Sci. U. S. A.* **89**, 5951–5955 (1992).
  48. Schenck, J. F. The role of magnetic susceptibility in magnetic resonance imaging: MRI magnetic compatibility of the first and second kinds. *Med. Phys.* **23**, 815–850 (1996).
  49. Kim, S.-G. & Ogawa, S. Biophysical and physiological origins of blood oxygenation level-dependent fMRI signals. *J. Cereb. Blood Flow Metab.* **32**,

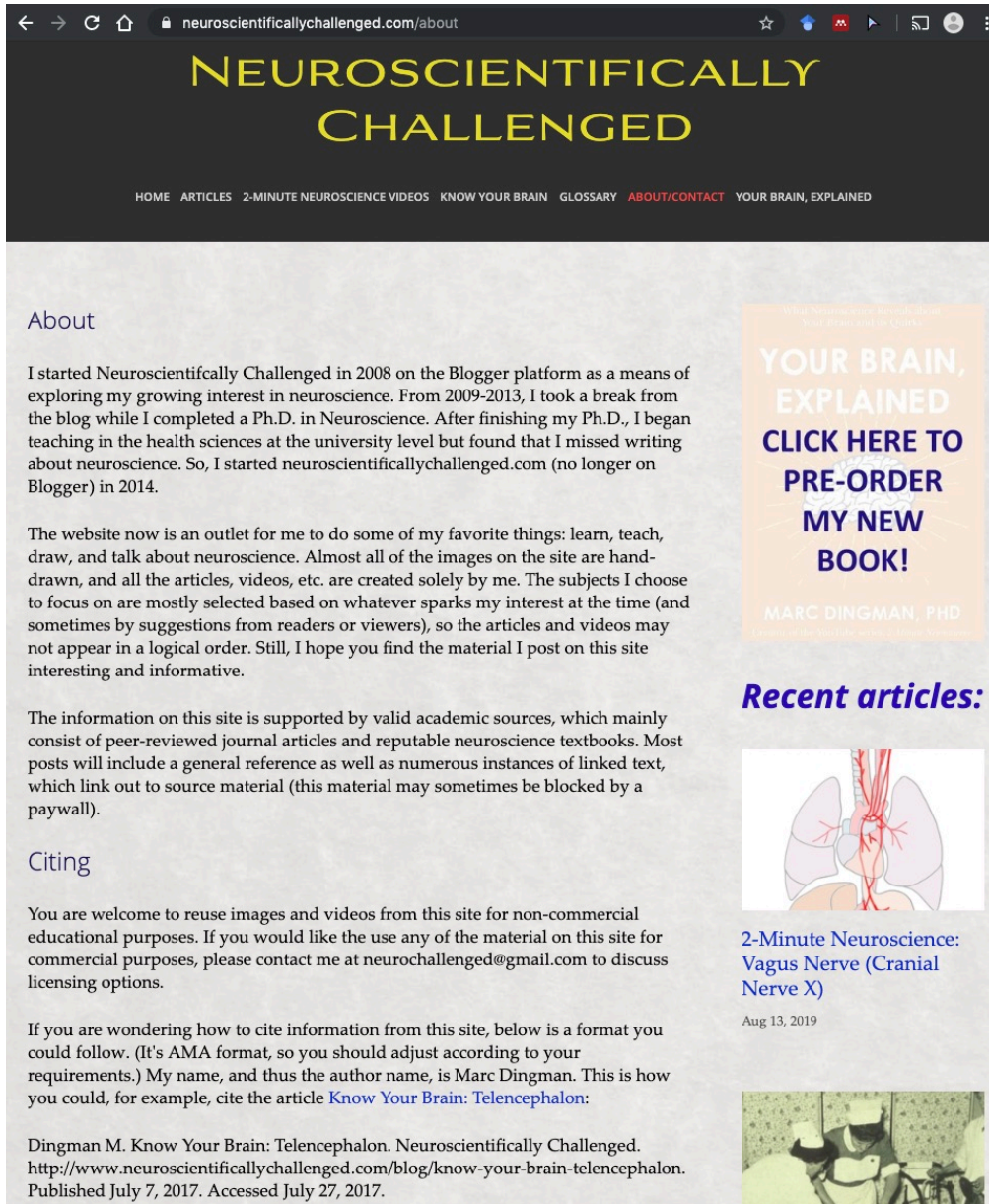
- 1188–1206 (2012).
50. Huettel, S. A., Song, A. W. & McCarthy, G. Chapter 5: MR Contrast Mechanisms and Pulse Sequences. in *Functional Magnetic Resonance Imaging* 121–157 (Sinauer Associates, Inc., 2009).
  51. Huettel, S. A., Song, A. W. & McCarthy, G. Chapter 6: From Neuronal to Hemodynamic Activity. in *Functional Magnetic Resonance Imaging* 159–192 (Sinauer Associates, Inc., 2009).
  52. Niedermeyer, E. Chapter 9: The Normal EEG of the Waking Adult. in *Electroencephalography : Basic principles, clinical applications, and related fields* 167–192 (Wolters Kluwer, 2004).
  53. Niedermeyer, E. Chapter 36: Depth Electroencephalography. in *Electroencephalography : Basic principles, clinical applications, and related fields* 733–748 (Wolters Kluwer, 2005).
  54. Ritter, P. & Villringer, A. Simultaneous EEG–fMRI. *Neurosci. Biobehav. Rev.* **30**, 823–838 (2006).
  55. Ferree, T. ., Clay, M. . & Tucker, D. . The spatial resolution of scalp EEG. *Neurocomputing* **38–40**, 1209–1216 (2001).
  56. Reilly, E. L. Chapter 7: EEG Recording and Operation of the Apparatus. in *Electroencephalography : Basic principles, clinical applications, and related fields* 139–159 (2005).
  57. Mulert, C. Chapter 5: What Can fMRI Add to the ERP Story? in *EEG-fMRI: Physiological Basis, Technique, and Applications* 83–95 (2010).
  58. Ives, J. R., Warach, S., Schmitt, F., Edelman, R. R. & Schomer, D. L. Monitoring the patient’s EEG during echo planar MRI. *Electroencephalogr. Clin. Neurophysiol.* **87**, 417–420 (1993).
  59. Huang-Hellinger, F. R. *et al.* Simultaneous functional magnetic resonance imaging and electrophysiological recording. *Hum. Brain Mapp.* **3**, 13–23 (1995).
  60. LeVan, P. & Gotman, J. Independent component analysis as a model-free approach for the detection of BOLD changes related to epileptic spikes: A simulation study. *Hum. Brain Mapp.* **30**, 2021–2031 (2009).
  61. Murta, T., Leal, A., Garrido, M. I. & Figueiredo, P. Dynamic Causal Modelling of epileptic seizure propagation pathways: A combined EEG–fMRI study. *Neuroimage* **62**, 1634–1642 (2012).
  62. Beres, A. M. Time is of the Essence: A Review of Electroencephalography (EEG) and Event-Related Brain Potentials (ERPs) in Language Research. *Appl. Psychophysiol. Biofeedback* **42**, 247–255 (2017).
  63. Carmichael, D. Chapter 10: Image Quality Issues. in *EEG-fMRI: Physiological Basis, Technique, and Applications* (eds. Mulert, C. & Lemieux, L.) 173–199 (Springer, 2010).
  64. Yan, W. X., Mullinger, K. J., Brookes, M. J. & Bowtell, R. Understanding gradient artefacts in simultaneous EEG/fMRI. *Neuroimage* **46**, 459–471 (2009).
  65. Allen, P. J. Chapter 7: EEG Instrumentation and Safety. in *EEG-fMRI: Physiological Basis, Technique, and Applications* (eds. Mulert, C. & Lemieux, L.) 115–133 (Springer, 2010).
  66. Debener, S., Kranczioch, C. & Gutberlet, I. Chapter 8: EEG Quality: Origin and Reduction of the EEG Cardiac-Related Artifact. in *EEG-fMRI: Physiological*

- Basis, Technique, and Applications* (eds. Mulert, C. & Lemieux, L.) 135–151 (Springer, 2010).
67. Ritter, P., Becker, R., Freyer, F. & Villringer, A. Chapter 9: EEG Quality: The Image Acquisition Artefact. in *EEG-fMRI: Physiological Basis, Technique, and Applications* (eds. Mulert, C. & Lemieux, L.) 153–171 (Springer, 2010).
  68. Felblinger, J., Slotboom, J., Kreis, R., Jung, B. & Boesch, C. Restoration of electrophysiological signals distorted by inductive effects of magnetic field gradients during MR sequences. *Magn. Reson. Med.* **41**, 715–721 (1999).
  69. Warach, S. *et al.* EEG-triggered echo-planar functional MRI in epilepsy. *Neurology* **47**, 89–93 (1996).
  70. Sommer, M., Meinhardt, J. & Volz, H.-P. *Combined Measurement of Event-Related Potentials (ERPs) and fMRI*. *Acta Neurobiol. Exp* **63**, (2003).
  71. Baudewig, J., Bittermann, H. ., Paulus, W. & Frahm, J. Simultaneous EEG and functional MRI of epileptic activity: a case report. *Clin. Neurophysiol.* **112**, 1196–1200 (2001).
  72. Krakow, K. *et al.* EEG-triggered functional MRI of interictal epileptiform activity in patients with partial seizures. *Brain* **122**, 1679–1688 (1999).
  73. Seeck, M. *et al.* Non-invasive epileptic focus localization using EEG-triggered functional MRI and electromagnetic tomography. *Electroencephalogr. Clin. Neurophysiol.* **106**, 508–512 (1998).
  74. Symms, M. R. *et al.* Reproducible localization of interictal epileptiform discharges using EEG-triggered fMRI. *Phys. Med. Biol.* **44**, N161–N168 (1999).
  75. Ritter, P., Becker, R., Graefe, C. & Villringer, A. Evaluating gradient artifact correction of EEG data acquired simultaneously with fMRI. *Magn. Reson. Imaging* **25**, 923–932 (2007).
  76. Mullinger, K. J., Castellone, P. & Bowtell, R. Best Current Practice for Obtaining High Quality EEG Data During Simultaneous fMRI. *J. Vis. Exp.* e50283 (2013). doi:10.3791/50283
  77. de Munck, J. C., van Houdt, P. J., Gonçalves, S. I., van Wegen, E. & Ossenblok, P. P. W. Novel artefact removal algorithms for co-registered EEG/fMRI based on selective averaging and subtraction. *Neuroimage* **64**, 407–415 (2013).
  78. Widrow, B. *et al.* Adaptive noise cancelling: Principles and applications. *Proc. IEEE* **63**, 1692–1716 (1975).
  79. Myers, P. S., McNeely, M. E., Pickett, K. A., Duncan, R. P. & Earhart, G. M. Effects of exercise on gait and motor imagery in people with Parkinson disease and freezing of gait. *Park. Relat. Disord.* **53**, 89–95 (2018).
  80. Griffiths, D. J. Chapter 1: The Wave Function. in *Introduction to Quantum Mechanics* 1–19 (Prentice Hall, 1995).
  81. Deift, P. & Trubowitz, E. Inverse scattering on the line. *Commun. Pure Appl. Math.* **32**, 121–251 (1979).
  82. Calogero, F. & Degasperis, A. *Spectral Transform and Solitons I*. (North-Holland, 1982).
  83. Helffer, B. & Laleg-Kirati, T. M. On semi-classical questions related to signal analysis. *Asymptot. Anal.* **75**, 125–144 (2011).
  84. Chahid, A., Serrai, H., Achten, E. & Laleg-Kirati, T.-M. A New ROI-Based performance evaluation method for image denoising using the Squared

- Eigenfunctions of the Schrödinger Operator. in *2018 40th Annual International Conference of the IEEE Engineering in Medicine and Biology Society (EMBC)* 5579–5582 (IEEE, 2018). doi:10.1109/EMBC.2018.8513615
85. Laleg-Kirati, T.-M., Zhang, J., Achten, E. & Serrai, H. Spectral data de-noising using semi-classical signal analysis: application to localized MRS. *NMR Biomed.* **29**, 1477–1485 (2016).
  86. Chahid, A. *et al.* Residual Water Suppression Using the Squared Eigenfunctions of the Schrödinger Operator. *IEEE Access* **7**, 69126–69137 (2019).
  87. Glaser, J., Beisteiner, R., Bauer, H. & Fischmeister, F. FACET – a “Flexible Artifact Correction and Evaluation Toolbox” for concurrently recorded EEG/fMRI data. *BMC Neurosci.* **14**, 138 (2013).
  88. Delorme, A. & Makeig, S. EEGLAB: an open source toolbox for analysis of single-trial EEG dynamics including independent component analysis. *J. Neurosci. Methods* **134**, 9–21 (2004).
  89. Laleg, T. M., Crépeau, E., Papelier, Y. & Sorine, M. Arterial blood pressure analysis based on scattering transform i. in *Annual International Conference of the IEEE Engineering in Medicine and Biology - Proceedings* 5326–5329 (2007). doi:10.1109/IEMBS.2007.4353544
  90. Laleg, T.-M., Medigue, C., Cottin, F. & Sorine, M. Arterial blood pressure analysis based on scattering transform II. in *2007 29th Annual International Conference of the IEEE Engineering in Medicine and Biology Society* 5330–5333 (IEEE, 2007). doi:10.1109/IEMBS.2007.4353545
  91. Peltonen, S., Gabbouj, M. & Astola, J. Nonlinear filter design: methodologies and challenges. in *ISPA 2001. Proceedings of the 2nd International Symposium on Image and Signal Processing and Analysis. In conjunction with 23rd International Conference on Information Technology Interfaces (IEEE Cat. No.01EX480)* 102–107 (Univ. Zagreb). doi:10.1109/ISPA.2001.938611
  92. Krylov, N. M. & Bogoliubov, N. N. *Introduction to non-linear mechanics.* (Princeton University Press, 1949).

# Appendices

## Appendix A: Permission for reproduction of scientific figures



The screenshot shows a web browser window with the URL neuroscientificallychallenged.com/about. The page has a dark header with the title "NEUROSCIENTIFICALLY CHALLENGED" in yellow. Below the header is a navigation menu with links: HOME, ARTICLES, 2-MINUTE NEUROSCIENCE VIDEOS, KNOW YOUR BRAIN, GLOSSARY, ABOUT/CONTACT (highlighted in red), and YOUR BRAIN, EXPLAINED. The main content area is light gray and contains several sections: "About", "Citing", and "Recent articles:". The "About" section describes the site's history and content. The "Citing" section provides information on how to cite the site's content. The "Recent articles:" section features a "2-Minute Neuroscience: Vagus Nerve (Cranial Nerve X)" article with a date of Aug 13, 2019, and a small image of a person on a bicycle. To the right of the "About" section is a promotional banner for the book "YOUR BRAIN, EXPLAINED" by Marc Dingman, PhD, with a "PRE-ORDER MY NEW BOOK!" call to action.

← → ↻ 🏠 🔒 neuroscientificallychallenged.com/about ☆ 📄 🔍 🗑️ ⋮

# NEUROSCIENTIFICALLY CHALLENGED

HOME ARTICLES 2-MINUTE NEUROSCIENCE VIDEOS KNOW YOUR BRAIN GLOSSARY **ABOUT/CONTACT** YOUR BRAIN, EXPLAINED

## About

I started Neuroscientifically Challenged in 2008 on the Blogger platform as a means of exploring my growing interest in neuroscience. From 2009-2013, I took a break from the blog while I completed a Ph.D. in Neuroscience. After finishing my Ph.D., I began teaching in the health sciences at the university level but found that I missed writing about neuroscience. So, I started neuroscientificallychallenged.com (no longer on Blogger) in 2014.

The website now is an outlet for me to do some of my favorite things: learn, teach, draw, and talk about neuroscience. Almost all of the images on the site are hand-drawn, and all the articles, videos, etc. are created solely by me. The subjects I choose to focus on are mostly selected based on whatever sparks my interest at the time (and sometimes by suggestions from readers or viewers), so the articles and videos may not appear in a logical order. Still, I hope you find the material I post on this site interesting and informative.

The information on this site is supported by valid academic sources, which mainly consist of peer-reviewed journal articles and reputable neuroscience textbooks. Most posts will include a general reference as well as numerous instances of linked text, which link out to source material (this material may sometimes be blocked by a paywall).

## Citing

You are welcome to reuse images and videos from this site for non-commercial educational purposes. If you would like the use any of the material on this site for commercial purposes, please contact me at neurochallenged@gmail.com to discuss licensing options.

If you are wondering how to cite information from this site, below is a format you could follow. (It's AMA format, so you should adjust according to your requirements.) My name, and thus the author name, is Marc Dingman. This is how you could, for example, cite the article [Know Your Brain: Telencephalon](#):

Dingman M. Know Your Brain: Telencephalon. Neuroscientifically Challenged. <http://www.neuroscientificallychallenged.com/blog/know-your-brain-telencephalon>. Published July 7, 2017. Accessed July 27, 2017.

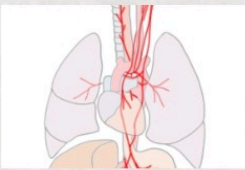
What Neuroscience Knowledge You Need to Know

## YOUR BRAIN, EXPLAINED

CLICK HERE TO PRE-ORDER MY NEW BOOK!

MARC DINGMAN, PHD

### Recent articles:



**2-Minute Neuroscience: Vagus Nerve (Cranial Nerve X)**

Aug 13, 2019



# QUESTIONS AND ANSWERS IN MRI

- Home
- Complete List of Questions
- ...Magnets & Scanners
- ...The NMR Phenomenon
- ...Pulse Sequences
- ...Making an Image
- ...K-space & Rapid Imaging
- ...Paramagnetic Contrast
- ...Cardiovascular and MRA
- ...MR Artifacts
- ...Functional Imaging
- ...MR Spectroscopy
- ...New/Advanced Topics
- ...Coming Soon!
- Copyright/Legal
- What's New
- Open Forum/Discussion
- Self-test Quizzes - NEW!

## Copyright Issues

During 30 years of radiology practice I have collected numerous cases, drawings, and illustrations relating to MR imaging and MR physics. Although most of these are of my own creation, a number of images, photographs, and graphic materials have come from colleagues in academics and industry. A number of these externally derived elements have been incorporated into this web site, and I have given full credit to these sources and/or obtained permission for their use when possible.

Unfortunately, the provenances surrounding some of these graphic elements collected over three decades have been lost or forgotten. It is not my intent to misuse anyone's copyrighted work, and I fully respect artist and content owner's rights. I pledge to fully comply with the [Digital Millenium Copyright Act of 1998](#), investigating any alleged infringement notices by the owner and removing any verified item or link promptly. To make such a notice, please click [here](#) and provide details. Alternatively, I would sincerely appreciate your allowing continued use of these materials on the site if you simply tell me how they should be credited.

In addition to graphic elements, this web site also contains links and pdfs to a number of scientific papers of which the original authors and publishers may retain copyrights. Many of these works are already widely available on the internet from the authors' own web sites or institutional repositories. A substantial number of papers and images are distributed under open access and Creative Commons licenses. Some very old works are now in the public domain. Others I have personally purchased or received as reprint gifts from authors over the years. As you read these papers on my web site, consider yourself as a student guest sitting in my private library that I maintain for teaching purposes. I would ask all readers of this site not to copy, repost, or distribute these works lest they be taken down and not available for the higher good of science education.

This web site has been created as a public service to the greater scientific community. I receive no compensation or external support for this endeavor and have personally assumed all costs of producing and maintaining this site. So, if an item is discovered that has unintentionally infringed on someone else's work, I ask understanding and forgiveness and promise to quickly make things right.

On the flip side, all other images and text on this website are my own creation, so any commercial use of this material without my express written consent is prohibited. However, **if you wish to use a small number of my images (in a non-commercial setting, such as for lectures, graduate theses, etc), feel free to do so, crediting them "Courtesy of Allen D. Elster, MRIquestions.com"**.

Allen Elster

**SPRINGER NATURE LICENSE  
TERMS AND CONDITIONS**

Aug 13, 2019

This Agreement between University of Western Ontario -- Gabriel Benigno ("You") and Springer Nature ("Springer Nature") consists of your license details and the terms and conditions provided by Springer Nature and Copyright Clearance Center.

License Number	4647090152001
License date	Aug 13, 2019
Licensed Content Publisher	Springer Nature
Licensed Content Publication	Springer eBook
Licensed Content Title	EEG Instrumentation and Safety
Licensed Content Author	Philip J. Allen
Licensed Content Date	Jan 1, 2009
Type of Use	Thesis/Dissertation
Requestor type	academic/university or research institute
Format	electronic
Portion	figures/tables/illustrations
Number of figures/tables/illustrations	1
Will you be translating?	no
Circulation/distribution	<501
Author of this Springer Nature content	no
Title	Thesis: Schrödinger filtering: a novel technique for removing gradient artifact from electroencephalography data acquired during functional magnetic resonance imaging
Institution name	University of Western Ontario
Expected presentation date	Jan 2020
Portions	figure 1
Requestor Location	University of Western Ontario 1151 Richmond St  London, ON N6A3K7 Canada Attn: University of Western Ontario
Total	0.00 USD

This agreement sets out the terms and conditions of the licence (the **Licence**) between you and **Springer Nature Customer Service Centre GmbH** (the **Licensor**). By clicking 'accept' and completing the transaction for the material (**Licensed Material**), you also confirm your acceptance of these terms and conditions.

**1. Grant of License**

- 1. 1.** The Licensor grants you a personal, non-exclusive, non-transferable, world-wide licence to reproduce the Licensed Material for the purpose specified in your order only. Licences are granted for the specific use requested in the order and for no other use, subject to the conditions below.
- 1. 2.** The Licensor warrants that it has, to the best of its knowledge, the rights to license reuse of the Licensed Material. However, you should ensure that the material you are requesting is original to the Licensor and does not carry the copyright of another entity (as credited in the published version).
- 1. 3.** If the credit line on any part of the material you have requested indicates that it was reprinted or adapted with permission from another source, then you should also seek permission from that source to reuse the material.

**2. Scope of Licence**

- 2. 1.** You may only use the Licensed Content in the manner and to the extent permitted by these Ts&Cs and any applicable laws.
- 2. 2.** A separate licence may be required for any additional use of the Licensed Material, e.g. where a licence has been purchased for print only use, separate permission must be obtained for electronic re-use. Similarly, a licence is only valid in the language selected and does not apply for editions in other languages unless additional translation rights have been granted separately in the licence. Any content owned by third parties are expressly excluded from the licence.
- 2. 3.** Similarly, rights for additional components such as custom editions and derivatives require additional permission and may be subject to an additional fee. Please apply to [Journalpermissions@springernature.com](mailto:Journalpermissions@springernature.com)/[bookpermissions@springernature.com](mailto:bookpermissions@springernature.com) for these rights.
- 2. 4.** Where permission has been granted **free of charge** for material in print, permission may also be granted for any electronic version of that work, provided that the material is incidental to your work as a whole and that the electronic version is essentially equivalent to, or substitutes for, the print version.
- 2. 5.** An alternative scope of licence may apply to signatories of the [STM Permissions Guidelines](#), as amended from time to time.

**3. Duration of Licence**

**3. 1.** A licence for is valid from the date of purchase ('Licence Date') at the end of the relevant period in the below table:

<b>Scope of Licence</b>	<b>Duration of Licence</b>
Post on a website	12 months
Presentations	12 months
Books and journals	Lifetime of the edition in the language purchased

#### 4. Acknowledgement

**4. 1.** The Licensor's permission must be acknowledged next to the Licenced Material in print. In electronic form, this acknowledgement must be visible at the same time as the figures/tables/illustrations or abstract, and must be hyperlinked to the journal/book's homepage. Our required acknowledgement format is in the Appendix below.

#### 5. Restrictions on use

**5. 1.** Use of the Licensed Material may be permitted for incidental promotional use and minor editing privileges e.g. minor adaptations of single figures, changes of format, colour and/or style where the adaptation is credited as set out in Appendix 1 below. Any other changes including but not limited to, cropping, adapting, omitting material that affect the meaning, intention or moral rights of the author are strictly prohibited.

**5. 2.** You must not use any Licensed Material as part of any design or trademark.

**5. 3.** Licensed Material may be used in Open Access Publications (OAP) before publication by Springer Nature, but any Licensed Material must be removed from OAP sites prior to final publication.

#### 6. Ownership of Rights

**6. 1.** Licensed Material remains the property of either Licensor or the relevant third party and any rights not explicitly granted herein are expressly reserved.

#### 7. Warranty

IN NO EVENT SHALL LICENSOR BE LIABLE TO YOU OR ANY OTHER PARTY OR ANY OTHER PERSON OR FOR ANY SPECIAL, CONSEQUENTIAL, INCIDENTAL OR INDIRECT DAMAGES, HOWEVER CAUSED, ARISING OUT OF OR IN CONNECTION WITH THE DOWNLOADING, VIEWING OR USE OF THE MATERIALS REGARDLESS OF THE FORM OF ACTION, WHETHER FOR BREACH OF CONTRACT, BREACH OF WARRANTY, TORT, NEGLIGENCE, INFRINGEMENT OR OTHERWISE (INCLUDING, WITHOUT LIMITATION, DAMAGES BASED ON LOSS OF PROFITS, DATA, FILES, USE, BUSINESS OPPORTUNITY OR CLAIMS OF THIRD PARTIES), AND WHETHER OR NOT THE PARTY HAS BEEN ADVISED OF THE POSSIBILITY OF SUCH DAMAGES. THIS LIMITATION SHALL APPLY NOTWITHSTANDING ANY FAILURE OF ESSENTIAL PURPOSE OF ANY LIMITED REMEDY PROVIDED HEREIN.

#### 8. Limitations

**8. 1. BOOKS ONLY:**Where 'reuse in a dissertation/thesis' has been selected the following terms apply: Print rights of the final author's accepted manuscript (for clarity, NOT the published version) for up to 100 copies, electronic rights for use only on a personal website or institutional repository as defined by the Sherpa guideline ([www.sherpa.ac.uk/romeo/](http://www.sherpa.ac.uk/romeo/)).

#### 9. Termination and Cancellation

9. 1. Licences will expire after the period shown in Clause 3 (above).
9. 2. Licensee reserves the right to terminate the Licence in the event that payment is not received in full or if there has been a breach of this agreement by you.

**Appendix 1 – Acknowledgements:**

**For Journal Content:**

Reprinted by permission from [the Licensor]: [Journal Publisher (e.g. Nature/Springer/Palgrave)] [JOURNAL NAME] [REFERENCE CITATION (Article name, Author(s) Name), [COPYRIGHT] (year of publication)]

**For Advance Online Publication papers:**

Reprinted by permission from [the Licensor]: [Journal Publisher (e.g. Nature/Springer/Palgrave)] [JOURNAL NAME] [REFERENCE CITATION (Article name, Author(s) Name), [COPYRIGHT] (year of publication), advance online publication, day month year (doi: 10.1038/sj.[JOURNAL ACRONYM].)]

**For Adaptations/Translations:**

Adapted/Translated by permission from [the Licensor]: [Journal Publisher (e.g. Nature/Springer/Palgrave)] [JOURNAL NAME] [REFERENCE CITATION (Article name, Author(s) Name), [COPYRIGHT] (year of publication)]

**Note: For any republication from the British Journal of Cancer, the following credit line style applies:**

Reprinted/adapted/translated by permission from [the Licensor]: on behalf of Cancer Research UK: : [Journal Publisher (e.g. Nature/Springer/Palgrave)] [JOURNAL NAME] [REFERENCE CITATION (Article name, Author(s) Name), [COPYRIGHT] (year of publication)]

**For Advance Online Publication papers:**

Reprinted by permission from The [the Licensor]: on behalf of Cancer Research UK: [Journal Publisher (e.g. Nature/Springer/Palgrave)] [JOURNAL NAME] [REFERENCE CITATION (Article name, Author(s) Name), [COPYRIGHT] (year of publication), advance online publication, day month year (doi: 10.1038/sj.[JOURNAL ACRONYM].)]

**For Book content:**

Reprinted/adapted by permission from [the Licensor]: [Book Publisher (e.g. Palgrave Macmillan, Springer etc)] [Book Title] by [Book author(s)] [COPYRIGHT] (year of publication)]

**Other Conditions:**

Version 1.2

Questions? [customer@copyright.com](mailto:customer@copyright.com) or +1-855-239-3415 (toll free in the US) or +1-978-646-2777.

# Curriculum vitae

**Name:** Gabriel Benigno

**Post-secondary Education and Degrees:** The University of Western Ontario  
London, Ontario, Canada  
2019 M.Sc. (Department of Medical Biophysics)

York University  
Toronto, Ontario, Canada  
2017 B.Sc. (Specialization in Biophysics with Honours)

**Honours and Awards:** Western Graduate Research Scholarship  
The University of Western Ontario  
2017-2019

Dean's Honour Roll  
York University  
2014-2015

Continuing Student Scholarship  
York University  
2015

**Related Work Experience** Graduate Research Assistant  
University of Western Ontario  
Sep 2017 – Apr 2019  
Dr. Ravi Menon  
Simultaneous ultrahigh-field fMRI & electrophysiology in the  
lightly anesthetized rat: the search for a resting-state  
hemodynamic response function

Undergraduate Research Assistant  
York University  
Fall 2016 – Winter 2017  
Dr. Pouya Rezai  
Cell Culture & Microfluidics

Undergraduate Research Assistant  
University of Waterloo  
May-Aug 2016  
Dr. Michael Tam  
Cellulose nanocrystals as sustainable flocculants for wastewater  
treatment

Biophysics Project Course  
York University  
Jan-Apr 2016  
Dr. Chris Bergevin  
Modelling the inner ear with the chaotic synchronization of analog  
circuits

Undergraduate Research Assistant  
York University  
May 2015 – Apr 2016  
Dr. A. Kumarakrishnan  
Laser electronics developer

**Publications and Conferences:**

Benigno, Gabriel B.; Menon, Ravi S.; Serrai, Hacene. (2019). Schrödinger filtering: a novel technique for removing gradient artifact from electroencephalography data acquired during functional magnetic resonance imaging. *NeuroImage*. (submitted)

2019, Robarts Research Retreat, Western University: Schrödinger filtering poster presentation.

2019, Neuroscience Research Day, Western University: Schrödinger filtering poster presentation.

AFNI Bootcamp 2018, National Institutes of Health, USA: week-long course for the neuroimaging software AFNI.

2018, London Imaging Discovery Day (London, Ontario, Canada). Poster Presentation: Can I pick your brain? Simultaneous electrical recording and fMRI during the resting state.